Journal of Energy Storage 55 (2022) 105778

Contents lists available at ScienceDirect

Journal of Energy Storage

journal homepage: www.elsevier.com/locate/est

Research papers

Cerium oxide nanosheets-based tertiary composites (CeO_2/ZnO/$ZnWO_4$) for supercapattery application and evaluation of faradic & non-faradic capacitive distribution by using Donn's model

Muhammad Ramzan Khawar [a], Naveed Akhtar Shad [b], Sajad Hussain [c], Yasir Javed [a,*], Muhammad Munir Sajid [d], Asim Jilani [e], Muhammad Faheem [c], Ali Asghar [a,f]

[a] Department of Physics, University of Agriculture, Faisalabad, Pakistan
[b] National Institute of Biotechnology and Genetic Engineering, Jhang Road, Faisalabad, Pakistan
[c] Department of Physics, Division of Science and Technology, University of Education Lahore, Pakistan
[d] Henan Key Laboratory of Photovoltaic Materials, School of Physics, Henan Normal University, Xinxiang 453007, China
[e] Center of Nanotechnology, King Abdul-Aziz University, Jeddah 21589, Saudi Arabia
[f] Additive Manufacturing Institute, Shenzhen University, Shenzhen 518060, China

ARTICLE INFO

Keywords:
Composite materials
Hydrothermal process
Electrochemical properties
Supercapattery

ABSTRACT

Batteries and supercapacitors are trending energy storage devices nowadays but the low energy density of supercapacitors and modest power density of batteries limit their applications for practical usage. Recently a new class of energy storage devices called supercapattery has emerged as an ultimate energy storage device which shows a hybrid storage mechanism of both battery and supercapacitor. In the present work, CeO_2-based binary and tertiary composites have been prepared by the facile hydrothermal method, characterized by different techniques, and applied as an electrode in supercapacitors and supercapattery. The X-ray diffraction patterns and EDX confirm the successful synthesis of tertiary composites with the average crystallite size of 26 nm while the SEM images show the randomly orientated nanosheets of CeO_2 loaded with ZnO and $ZnWO_4$ over it. The XPS spectrum depicts the presence of variable oxidation states of cerium (Ce^{+2} and Ce^{+4}) in the tertiary composites. The electrochemical performance shows the highest specific capacity (496.9 Cg^{-1}) for tertiary composite. The supercapattery device is fabricated by using mixed (AC/Ternary composite) as a working electrode and AC as a cathode which is separated by filter paper. The evaluation of capacitive and battery mechanisms shows the dominant feature of diffusive and surface-controlled processes at lower and high scan rates respectively due to varying diffusion time of electrolyte species. The fabricated device shows the energy density and power density of 56.92 $Whkg^{-1}$ and 2000 Wkg^{-1} at a current density of 0.5 mAg^{-1} respectively with 88 % cyclic stability and 82 % coulombic efficiency.

1. Introduction

The rapid evolution of modern energy storage devices is offering ample options for traditional ways such as oil, coal, natural gas, and nuclear resources coal for energy harvesting [1,2]. The traditional energy sources create an alarming situation for the environment due to carbon emission, therefore, it is the need of the hour to investigate new environment-friendly energy sources such as wind energy, solar energy, lithium battery, and hydrogen energy [3–10]. Batteries and capacitors are conventional energy storage devices, however, have certain drawbacks i.e. low power density and energy density and reduced cyclability [11–13]. Due to these limitations, supercapacitors have gained much attention thanks to their high-power density and rapid charging [14–19]. Supercapacitors have better cyclability, low maintenance, environmental-friendly, and long-life cycle than other energy storage devices [20].

The electrode is the key component in any energy storage instrument. The electrode material contributes effectively to the charging-discharging process of the supercapacitor. Based on the charging-discharging mechanisms, supercapacitors are categorized into two groups; electrical double-layer capacitors and pseudo capacitors [21,22]. In a double-layer capacitor, electrodes are usually made up of

* Corresponding author.
E-mail addresses: myasi60@hotmail.com, yasir.javed@uaf.edu.pk (Y. Javed).

https://doi.org/10.1016/j.est.2022.105778
Received 21 July 2022; Received in revised form 16 September 2022; Accepted 26 September 2022
Available online 1 October 2022

carbon or carbon derivatives (Graphene, Fluorene, etc.) and separated by an inert porous sheet. The accumulation of positive and negative charges at the electrode interface makes enhanced surface area Helmholtz and diffusion layers which results in high power density. Whereas, for pseudo-capacitors, activated carbon electrode is generally mixed with metal oxides to increase the specific capacitance. For pseudo-capacitance, a Faradic charge mechanism occurs between the electrolyte and porous electrode through a redox reaction. In recent years, a lot of pristine and composite nanomaterials have been proposed as electrode materials e.g. RuO_2, MnO_2 [23,24] for pseudo-capacitor. The carbon-based electrode material is one of the most fascinating materials for supercapacitor applications due to its large surface area which ultimately provides a higher ion transfer ratio in the electrolyte [25]. A lot of metal oxides with graphene composites such as r-GO/CeO_2, GO/NiO [26], GO/CuO [27], rGO/TiO_2 [28], GO/MnO_2 [29] have been presented due to the excellent electrical properties, simple synthesis, and environment-friendly nature. Although supercapacitors have enormous potential for energy storage, less energy density is one of the major causes which limits their practical use. Recently, a new hybrid energy storage device, supercapattery is getting attention because that uses the principle of both supercapacitor and battery. In this device, the cathode (usually made up of carbonaceous material) is used to provide high energy density while the anode (pseudo behavior materials) for high power density. The supercapattery device not only provides higher power density but also offers comparatively higher energy density than the supercapacitor [30].

Cerium oxide (CeO_2) nanoparticles (NPs) are one of the potential materials for supercapacitor applications due to their binary transition state (Ce (IV)/Ce(III)) [31]. This binary transition state causes the rapid redox reaction in cerium and electrolyte ions. CeO_2 NPs depict higher retention rate, excellent recyclability, low toxicity and high catalytic property [32–34]. The only disadvantage of CeO_2 is its low conductivity which limits its practical applications. [35]. Several attempts have been made to increase the conductivity and specific capacitance of CeO_2. For example, Jeyaranjan et al. [36] synthesized the ternary hierarchical microspheres structure PANI/rGO/CeO_2 composite having a specific energy density of 46.27 $Whkg^{-1}$ and power density of 850 Wkg^{-1} with a 92 % retention rate. Prasanna et al. [37] modified the electrical conductivity of pristine CeO_2 by increasing the oxygen vacancies via the combustion method which showed a specific capacitance of 134.6 Fg^{-1}. Ojha et al. prepared CeO_2 modified MnO_2/RGO nanorods which depicted the higher specific capacitance (648 Fg^{-1}) than pristine MnO_2 [38]. CeO_2/ZnO composites have been reported for several applications such as sensing [39], photocatalytic degradation [40], and supercapacitors [41]. Arunpandiyan et al. [42] reported the CeO_2/ZnO composites as electrode materials with specific capacitance and energy density of 1069 Fg^{-1} and 39.6 $Whkg^{-1}$ respectively. Xie et al. [43] reported the CeO_2/ZnO composites for oxidation of carbon monoxide. Similarly, Qiao et al. [44] achieved the maximum power density of 1055 mW cm^{-2} for solid oxide fuel cell applications.

Several studies have shown that $ZnWO_4$ is highly stable as electrode material in energy storage devices. For example, Dhanush et al. [45] attained a 92 % retention rate for graphene-modified zinc tungstate electrodes in supercapacitor applications. Soultati et al. [46] observed the enhanced stability of pristine ZnO when it is modified with $ZnWO_4$ for usage as an electron extraction layer in organic solar cells. Recently, tungstate-based ternary nanocomposites are also being used due to their enormous properties. Sedighi et al. [47] prepared ternary $Ce_2W_2O_9$/$CoWO_4$/Porous carbon-based electrodes and achieved 70 % more power density (660 $mAhg^{-1}$) as compared to the binary $Ce_2W_2O_9$/$CoWO_4$ composites. Similarly, Kumar et al. [48] reported WS_2/$FeCo_2O_4$/activated carbon composites for high-performance battery grade anode material with 98 % retention for supercapacitor applications. Ali et al. [49] studied the diffusion and surface-controlled mechanism for porous zinc-based MOF material for supercapattery application. The hierarchical type fabricated electrodes have a maximum capacity of 172 C/g along with an excellent energy density and power density of 38.05 Wh/kg and 240 W/kg respectively. By following the same approach, Prabakaran and co-worker [50] studied the supercapattery behavior of tungstate-based materials (rGO-$CuWO_4$) which depicts the maximum specific capacity of 158.1 C g^{-1} at 2 Ag^{-1}. Although remarkable progress has been achieved by the authors to get maximum energy density and power density, the charge storage mechanism is required to be further analyzed. In the present work, low-cost and fine thin nano-sheets of CeO_2 composited with ZnO and $ZnWO_4$ have been prepared for supercapattery application by using a simple hydrothermal route. The basic motive of the study was to integrate the electrochemical properties of CeO_2/ZnO composite with highly stable $ZnWO_4$ to achieve the maximum power density, energy density, and stability. The fabricated supercapattery device provides the maximum energy density and power density of 56.92 $Whkg^{-1}$ and 2000 Wkg^{-1} respectively with 88 % retention capability and 82 % coulombic efficiency.

2. Experimental section

2.1. Materials

All the materials of analytical grade were purchased through a local supplier and used as received without any further purification. For the preparation of all derivatives of Zinc, Zinc acetate dihydrate ($C_4H_6O_4Zn{\cdot}2H_2O$, Purity 98 %) was used. Similarly, for the preparation of composite materials, cerium (III) chloride heptahydrate ($CeCl_3{\cdot}7H_2O$, purity 99 %) and sodium tungstate dihydrate ($Na_2WO_4{\cdot}2H_2O$, Purity 98 %) were used as primary precursors. While other chemicals like cetyltrimethylammonium bromide (CTAB, Purity 99 %), sodium hydroxide (NaOH, Purity 99 %), and potassium hydroxide (KOH, Purity 99 %) were used as secondary materials. For the preparation of electrodes, Nickel foam (6 mm thickness, 99.5 % purity) was used.

2.2. Preparation of electrode materials

Cerium oxide nanomaterials (CeO_2) were prepared by using the hydrothermal method. Cerium chloride heptahydrate (0.5 M) was dissolved into 100 ml distilled water and stirred for 15 min. The pH was maintained at 13 by adding 0.5 M NaOH solution. After constant stirring for 1 h, 0.5 g of CTAB was added as a stabilizing agent. The final prepared solution was shifted into Teflon lined autoclave for hydrothermal treatment at 220 °C temperature for 16 h. The color of the synthesized product changed from white to sand white which indicated the successful reaction. The suspension so formed, was then washed and dried. The final product was further annealed at 500 °C temperature for 2 h and collected for further use in the synthesis of composites [51]. The pristine ZnO and $ZnWO_4$ were prepared by the same method by using zinc acetate and sodium tungstate dihydrate as precursors. For binary composites, the CeO_2 and ZnO were mixed with a 1:2 wt% ratio, and tertiary composites were prepared by mixing CeO_2, ZnO, and $ZnWO_4$ with a ratio of 1:2:3 wt% respectively under hydrothermal treatment.

2.3. Characterization tools

To investigate the structural composition, analysis was carried out by using a general-purpose X-Ray diffractometer (pXRD) DRON-8 with Cu kα = 0.154 nm and angle range 2θ = 20°–80°. The morphology of the synthesized materials was studied by using SEM (FEI, model Nove NanoSEM 450). Similarly, optical properties were studied by using Photoluminescence spectroscopy. Surface and functional analysis were performed by X-ray photoelectron spectroscopy (PHI-VersaProbII, PHI, Chanhassen, MN, USA) under a high vacuum (10^{-7} Pa). The formulas (1)–(3) are used for the structural analysis;

$$\text{Crystallite size (Scherrer's formula)}\ \ D = \frac{k\lambda}{\beta\cos\Theta} \quad (1)$$

$$\text{Williamson} - \text{Hall equation} \quad \beta\cos\Theta = \frac{k\lambda}{D} + 4\varepsilon\sin\theta \tag{2}$$

$$\text{Level of crystallinity; Crystallinity } (\%) = \frac{\text{Area of crystalline peaks}}{\text{Area of all peaks (crystalline + amorhous)}} \times 100 \tag{3}$$

where D is crystallite size, k is the shape factor, λ is the wavelength of X-rays (0.154 nm), β is full width at half maximum, and θ is the corresponding peak position in degrees.

2.4. Electrochemical measurements

The electrochemical characterization was performed by using three and two-electrode systems. The $Ag/AgCl_2$ and platinum wire was used as reference and counter electrodes respectively. The 2 M potassium hydroxide (KOH) solution was used as an electrolyte. Cyclic voltammetry, galvanostatic charging-discharging, and electrochemical impedance spectroscopy characterizations were performed by using the CS310 Electrochemical workstation.

2.5. Preparation of electrodes

The electrodes were prepared by using the synthesized material, activated carbon, and polyvinyl alcohol (PVA) in a 16:3:1 ratio. The mixture was initially blended well by the continuous addition of PVA solution. The slurry-like mixture was then spin-coated (100 rpm for 5 min) over the nickel foam. The advantage of spin coating over the other methods is the penetration of materials more efficiently into the pores of Ni foam. The coated Ni foam was then annealed at 100 °C for 10 min. The digital photographs of different steps performed for electrode preparation are shown in (Fig. 1).

3. Results and discussion

3.1. Materials characterization

Structural studies were carried out to confirm the phases of different composite materials. The XRD patterns of CeO_2, CeO_2/ZnO, and CeO_2/ZnO/$ZnWO_4$ composites are shown in Fig. 2. In the case of cerium oxide, all the diffraction peaks matched with the JCPDS Card # 01-081-079. The peaks observed at diffraction angles 28.54°, 33.07°, 47.47°, 57.33°, 59.07°, 69.40°, 76.68° and 79.06° correspond to (111), (200), (220), (311), (222), (400), (331) and (420) planes respectively [52]. The structure corresponds to the cubic phase with Fm3m space group. The narrow width of peaks corresponds to the higher crystallinity of the material. In the case of CeO_2/ZnO composites, both peaks for CeO_2 and ZnO are depicted in the spectrum, however, CeO_2 peaks are slightly shifted indicating the formation of composite materials. The peaks of ZnO are matched with the JCPDS card # 01-076-0704 having a

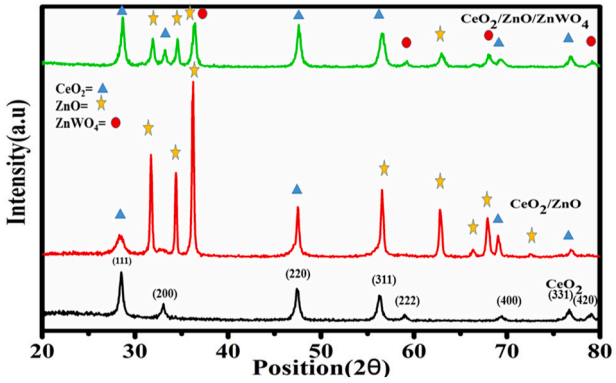

Fig. 2. XRD patterns of CeO_2, CeO_2/ZnO, and CeO_2/ZnO/$ZnWO_4$ composites in the range of 20° to 80° using Cu Kα X rays with wavelength 1.54 Å.

hexagonal structure whereas CeO_2 peaks are matched with the same cubic phase. The tertiary composites indicate the presence of CeO_2, ZnO, and $ZnWO_4$ diffraction peaks in the spectrum. The $ZnWO_4$ peaks are located at 36.3°, 58.8°, 68°, and 79.1° belong to (021), (300), (320), and (014) planes respectively with monoclinic phase and JCPDS card # 01-073-0554. The different structural parameters have also been calculated using relations (Eqs. (1)–(3)) provided in the Experimental section. Table 1 provides the value of crystallite size calculated by Debye-Scherrer's formula (highest intensity peak in each case), Williamson Hall plot, and level of crystallinity of the synthesized materials. Debye-Scherrer's method shows the crystallite size of pristine CeO_2, CeO_2/ZnO, and CeO_2/ZnO/$ZnWO_4$ composites as 25, 44, and 31 nm respectively. Williamson Hall method counts the crystal defects present in the material for crystallite size determination that have a certain effect due to strain induced in the lattice. The crystallite size determined by the Williamson-Hall method for CeO_2/ZnO composite is 21 nm which shows that crystal defects induce compressive stress in the atomic layers and shrink the crystallite size. Additionally, the presence of excess volume near grain boundaries (Ce^{3+}) also induces a stress field which results in a decrease in crystallite size [53]. In the case of pristine CeO_2 and tertiary composite, crystallite sizes increase to 32 nm and 52 nm respectively as

Table 1
Crystalline size and percentage crystallinity of all the materials.

Samples	Crystallite size (nm)		Level of crystallinity (%)
	Debye-Scherrer's method	Williamson-Hall method	
CeO_2	25	32	62
CeO_2/ZnO	44	21	65
CeO_2/ZnO/$ZnWO_4$	31	52	69

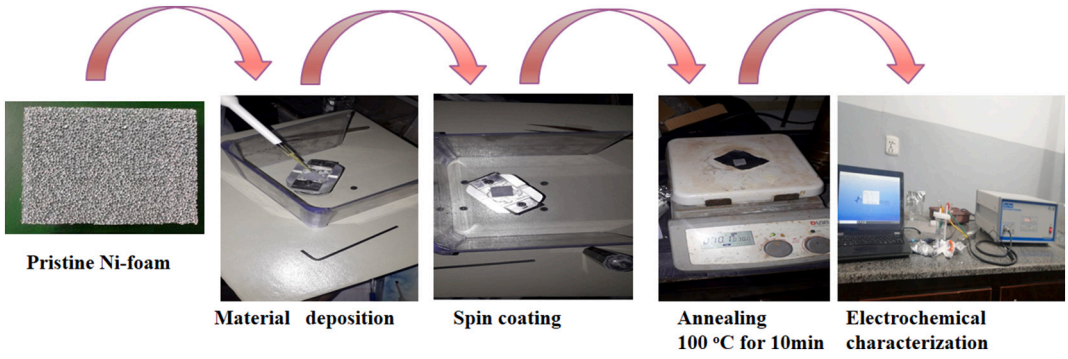

Fig. 1. Step-by-step procedure of the preparation of electrodes.

compared to Scherrer's formula, indicating the crystal expansion due to the crystal imperfections. The percentage crystallinity is also determined for different materials and it is observed that tertiary composites have the highest crystallinity (69 %) as compared to binary composites (65 %) and pristine CeO_2 (62 %) nanomaterials (Table 1).

The scanning electron microscopy images of pristine CeO_2, binary and ternary composites are shown in Fig. 3. Fig. 3a shows two-dimensional nanosheets with random orientation i.e. vertically and horizontally aligned. The pristine ZnO and $ZnWO_4$ have aggregate-like irregular morphologies (Fig. 3(b–c)). For binary composite (ZnO/CeO_2), particles are mostly agglomerated which are loaded over each other (Fig. 3d) and have flake-like morphologies. Whereas, in the case of tertiary composites, most of the nanosheets are decorated by ZnO and $ZnWO_4$ nanoparticles (Fig. 3e). The presence of 2D sheet-like morphologies of CeO_2 provides a large surface area for redox reaction and more exposed oxygen vacancies which result in enhanced specific capacitance of the prepared material [54]. The small granules of ZnO and $ZnWO_4$ embedded on 2D nanosheets also provide more surface defects in the composite materials. The direct interface of 2D nanosheets can promote electrons transportation rate between the electrode and electrolyte thus providing more conductive pathways [55]. The chemical composition of the tertiary composite materials is further confirmed by EDX analysis (Fig. 3f). The presence of Ce, Zn, W, and C peaks further supports the XRD results. The presence of carbon peak is due to the substrate used for SEM analysis. The wt% and at.% of different elements are determined and provided in Table 2. The high at.% of Ce and Zn species is favorable for fast redox reactions. The increased number of redox atoms facilitates the high ions conductivity which results in less charge transfer time [56]. The chemical distribution of different elements in the tertiary composites is further confirmed by EDX chemical mapping. The maps for different elements show the homogenous chemical distribution in the tertiary composites (Fig. 4(a–f)).

The photoluminescence (PL) spectra of pristine CeO_2 and its composites are recorded with 350 nm excitation wavelength and shown in Fig. 5. Intensity is significantly increased for binary and tertiary composites which may be attributed to the rapid excitonic recombination [57]. The first excitation peak is observed at 414 nm in all cases which is due to the transition by Ce 4f to O 2p [58]. The PL spectrum shows the oxygen vacancy mediation in the case of CeO_2. The wide spectrum of

Table 2
Weight% and atomic% of different elements present in the tertiary composites determined by EDX.

Element	Weight%	Atomic%
C	4.38	16.91
O	13.89	40.24
W	2.31	1.12
Ce	37.65	12.1
Zn	41.77	29.63

CeO_2 might be due to the defects present in the energy levels below the 4f band of oxygen vacancies. The higher PL intensity in the case of the binary and tertiary composite may be linked with the higher capacity to store oxygen vacancies due to the different transition states of Ce (III and IV) and Zn (II and III) [59]. In the case of tertiary composites, maximum PL intensity is observed with an additional peak near 510 nm that may be correlated with the blue emission band [60]. The presence of a second peak in the tertiary composites is attributed to the presence of tungstate species [61].

The surface elemental analysis with valance state study for tertiary composites is conducted through XPS and shown in Fig. 6. All the primary elemental peaks are present in the survey spectrum which further confirms composite formation (Fig. 6a). The Auger peaks are observed at 496.35 eV and 837 eV corresponds to Zn LMM and Ce MNN [62]. In tertiary composites, the B-site metal ions (Ce, Zn) with variable oxidation states are present. The oxidation/reduction state of oxygen atoms facilitates the rapid transfer of electrons which supports the battery-type behavior [63,64]. The variable oxidation states of cerium ions are confirmed as shown in the high-resolution spectrum of Ce 3d (Fig. 6b). The characteristic peaks of Ce^{4+} $3d_{5/2}$ are present at binding energies of 887.21 eV and 883.12 eV. Similarly, the satellite peaks for Ce^{3+} $3d_{3/2}$ are present at 898.74 eV, 909.34 eV and 917.12 eV. The relative percentage of different reduction states of cerium ions is calculated by using the formulas (4)–(5) [65].

$$[Ce^{4+}] = [Ce^{4+}]/[[Ce^{4+}] + [Ce^{3+}]] \quad (4)$$

and

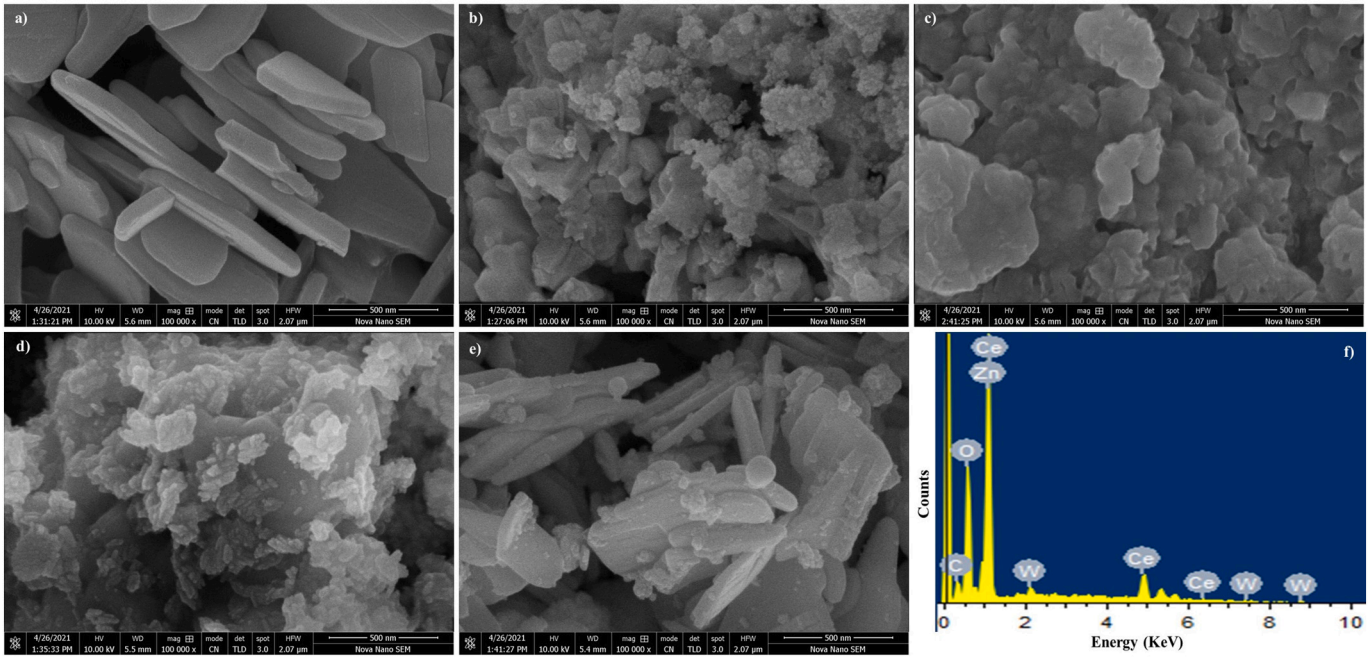

Fig. 3. SEM images; (a) CeO_2, (b) ZnO, (c) $ZnWO_4$, (d) CeO_2/ZnO composites, (e) CeO_2/ZnO/$ZnWO_4$, (f) EDX spectrum of tertiary composite.

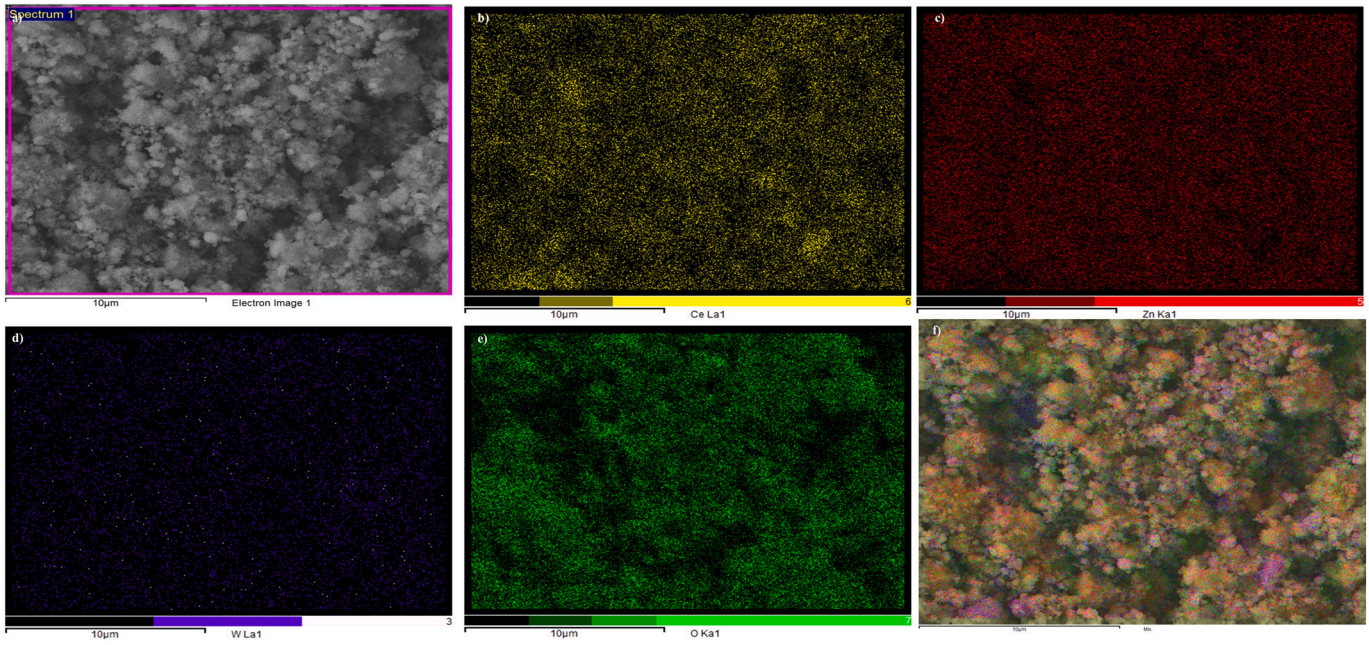

Fig. 4. EDX chemical mapping: (a) SEM image of the selected area, chemical maps of (b) Ce, (c) Zn, (d) W, (e) O, (f) Overlay image of the chemical maps.

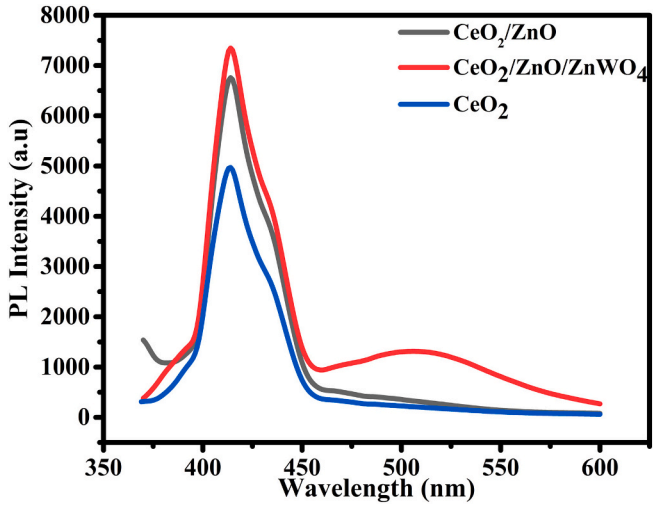

Fig. 5. Photoluminescence spectra of synthesized materials using laser light with an excitation wavelength of 350 nm.

$$[Ce^{3+}] = [Ce^{3+}]/[[Ce^{4+}] + [Ce^{3+}]] \quad (5)$$

The calculated percentage for Ce^{3+} and Ce^{4+} is 40 % and 60 % respectively. The tetravalent state of cerium ions may be due to the rapid oxidation with oxygen species [66]. This shows that tetravalent vacancies are more dominant in the formation of the tertiary composite. Similarly for ZnO, the characteristic peaks of Zn $2p_{3/2}$ and Zn $2p_{1/2}$ are present at 1021.73 eV and 1044.97 eV binding energies respectively which indicates the Zn^{2+} oxidation state of zinc ions (Fig. 6c) [67]. The core level tungstate species (W 4f) deconvolute into two peaks at 34.12 eV and 36.56 eV which can be assigned to W $4f_{7/2}$ and W $4f_{5/2}$ respectively (Fig. 6d) [68]. The binding energies for lattice oxygen and oxygen vacancies are located at 529.21 and 532.10 eV respectively (Fig. 6e) [65]. The percentage of lattice oxygen and oxygen vacancies are equal, calculated by the same method as described above.

3.2. Electrochemical studies

The charge storage nature and capacitive behavior were studied by cyclic voltammetry (CV) curves. The optimum potential window in all cases was from 0 to 0.7 V. The CV curves for different materials-based electrodes are shown in Fig. 7a–c. The samples were analyzed by varying scan rates ranging from 5 mV/s to 50 mV/s. The non-rectangular shape and sharp redox peaks of CV curves in all the cases depict the pseudo-capacitive nature of the materials [69]. In the case of pristine CeO_2, oxidation and reduction peaks in the redox reaction may be attributed to the double valance state of cerium ions (Ce^{+3} and Ce^{+4}) (Fig. 7a). The variable oxidation states of cerium ions are mainly responsible for the reversible reaction in the CV curve [70]. The addition of ZnO in CeO2 significantly enhances the integral CV area, evidencing the successful incorporation of Zinc ions with the Cerium ions (Fig. 7b). This incorporation may also cause additional benefit of less dissolution of Cerium ions in the electrolyte and enhances the conductivity as reported by [51,71]. Of the three materials, oxidation and reduction currents of tertiary composites are highest (±62 mA) at a scan rate of 50 mV/s (Fig. 7c). Even at higher scan rates, no significant change in the shape of CV is observed except the shifting of redox peak towards the further anodic and cathodic potential. This shift may be attributed to concentration polarization and electrochemical polarization [72].

The specific capacity of the material is calculated by using the following relation (6).

$$Qs = \frac{\int_{V_c}^{V_a} I \times VdV}{m \times S} \quad (6)$$

Qs = specific capacity (Cg^{-1}), m = mass loaded (mg), S = scan rate, $\int_{V_c}^{V_a} I \times dV$ = Area under the curve.

The minimum specific capacity is observed for CeO_2 which is 85.18 Cg^{-1} at a scan rate of 5 mV/S. The binary and tertiary composites have specific capacities of 202 Cg^{-1} and 496.9 Cg^{-1} respectively at a scan rate of 5 mV/S. The specific capacity decreases from a low scan rate to a fast scan rate due to more diffusion time for electrolytic ions to penetrate the pores of the material. At fast scan rates, only surface atoms of the electrode take part in the redox reaction, consequently, decreasing the specific capacity [73]. The improved specific capacity might be due to the synergy effect. The specific capacity in the case of CeO_2/ZnO

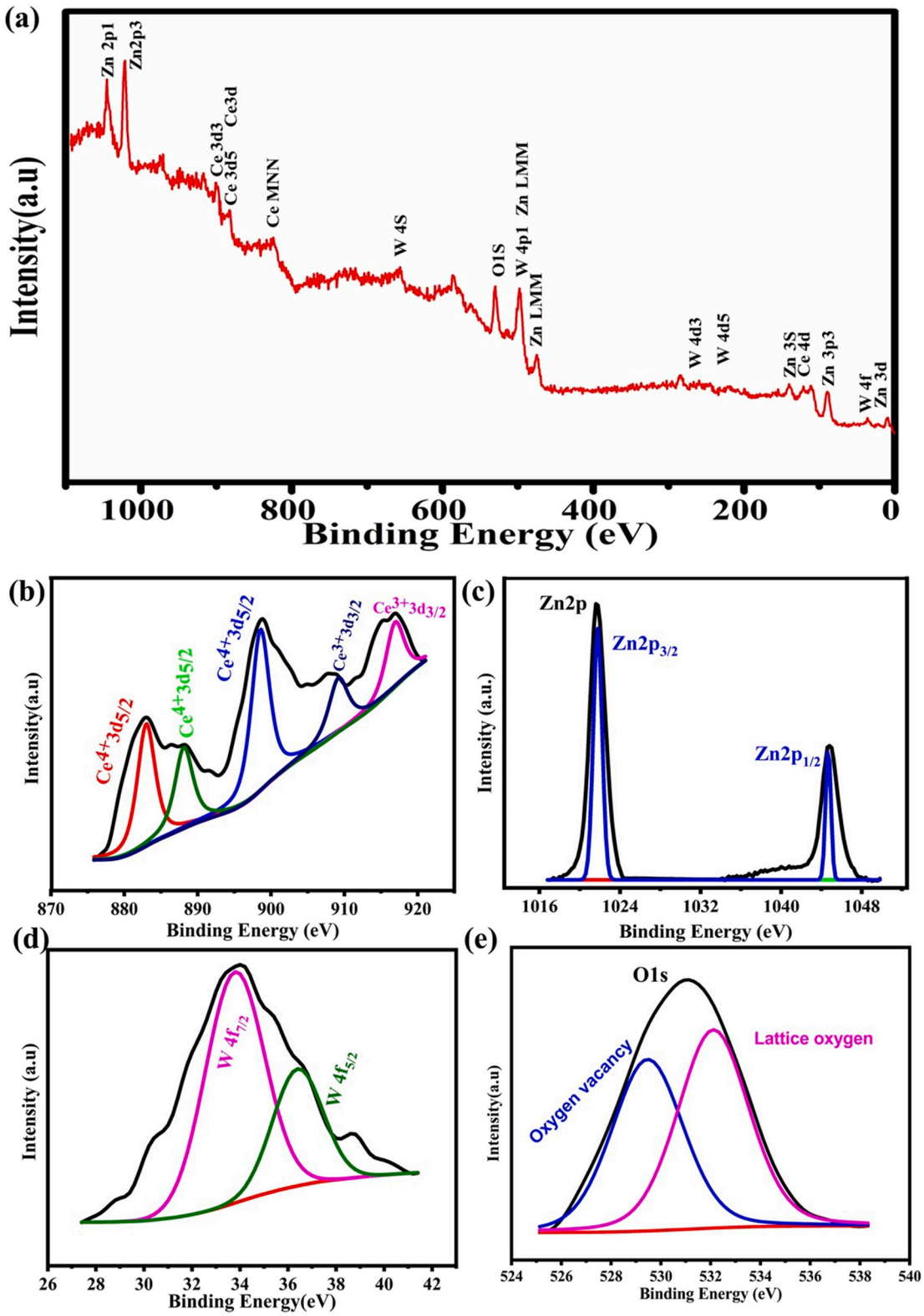

Fig. 6. XPS analysis of tertiary composite; (a) XPS survey scan of tertiary composite, High-resolution spectra of (b) Ce 3d, (c) Zn 2p, (d) W 4f, (e) O 1s.

composite may be linked with the increase in the number of valance states [74]. The larger surface area and high porosity of the CeO_2/ZnO composite can also lead to a higher specific capacity [71]. The high redox nature of nano ZnO is due to its variable valence state changes (transition between Zn (II)/Zn (III)). The surface defects may also be responsible for the pseudocapacitive nature of the ZnO [75]. Similarly, in the case of tertiary composites, WO_4^{-2} remains inactive during the reaction but increases the conducting channels for electrolytic ions which increases specific capacity [76]. The Zn (II) oxidation state is also responsible for the fast reversible reaction and pseudo-capacitive nature of the material along with variable Ce oxidation states [77]. In ternary composites, the presence of ZnO species provides more nucleation sites

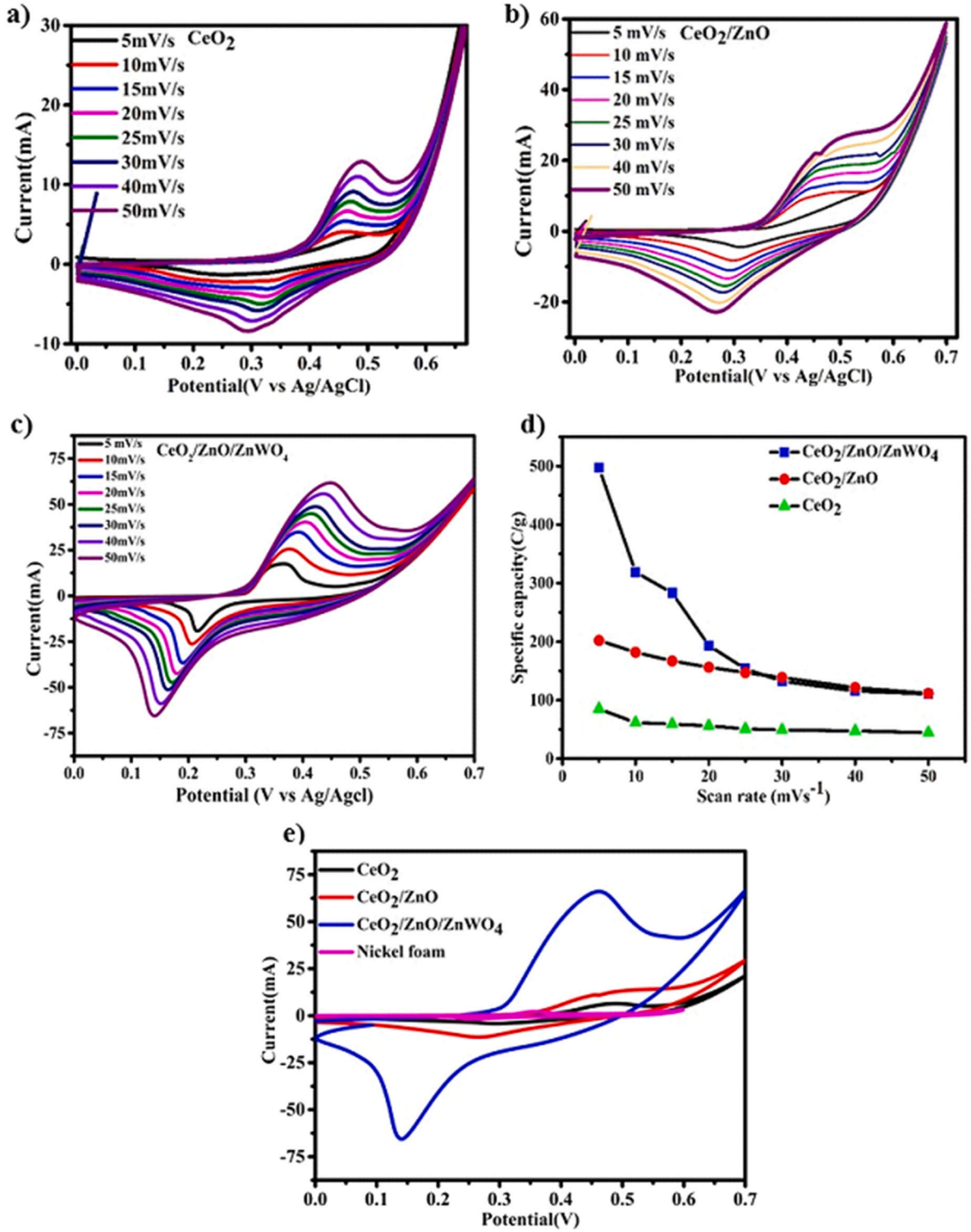

Fig. 7. CV curves of (a) CeO_2, (b) CeO_2/ZnO, (c) CeO_2/ZnO/$ZnWO_4$, (d) specific capacitance at different scan rates, (e) comparison of CV curves of different materials with Ni foam at scan rate 30 mV/s.

and enhances the surface area, ultimately yielding in stable structure than pristine materials. The possible charge storage mechanism is shown in Fig. 8. Keeping in view the above discussion it can be concluded that

I. The nanosheet-like morphology provides a larger specific area for reaction, thus offering more active sites for redox reactions.

II. The presence of CeO_2 with ZnO material not only increases the specific capacity of pristine CeO_2 but also increases the stability of the material as reported by [51].

III. The presence of tungstate species increases the conducting channels of the material which lowers the electrochemical series resistance (ESR) and increases the specific capacity.

The comparative CV curves of nickel foam and different materials

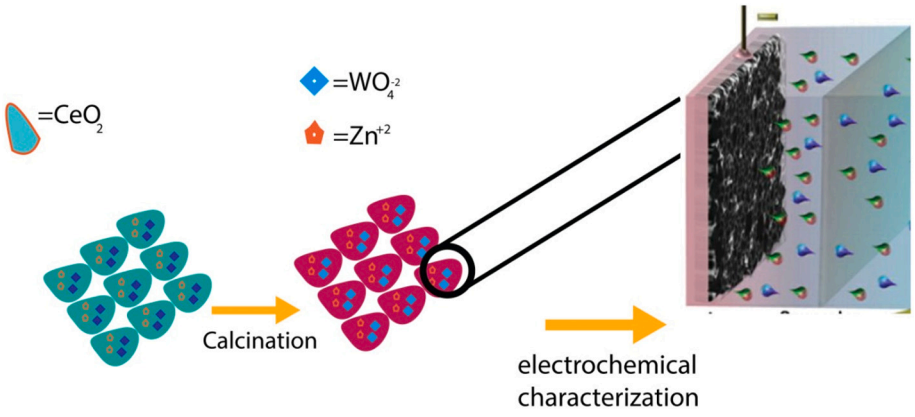

Fig. 8. The possible charge storage mechanism of $CeO_2/ZnO/ZnWO_4$ tertiary composites.

deposited on nickel foam at a scan rate of 30 mV/S are shown in Fig. 7e. The nickel foam has negligible contribution towards the charge storage mechanism and acts just as a current collector whereas deposited material offers CV response at the given scan rate. The possible contribution might consist of the following steps [78];

First, adsorption of K^+ ions at the electrode interface, and secondly, intercalation/deintercalation of K^+ ions in the pores and on the surface of CeO_2 nanosheets.

The faradic and non-faradic processes may involve the following reactions

$$\text{Faradic}: Ce^{IV}O_2 + K^+ + e^- \leftrightarrow Ce^{III}O{\cdot}O\,K^+ \text{ (Diffusive)}$$

$$\text{Non}-\text{faradic}: (CeO_2)\text{ surface} + K^+ + e^- \leftrightarrow (CeO_2{\cdot}K^+)\text{ surface (Capacitive)}$$

The current contribution due to faradic and non-faradic mechanisms for each material can be evaluated by plotting the graph (I_p vs $\upsilon^{1/2}$) and (I_p vs υ) respectively.

For faradic or diffusion-controlled mechanisms, the Eqs. (7)–(8) can be used

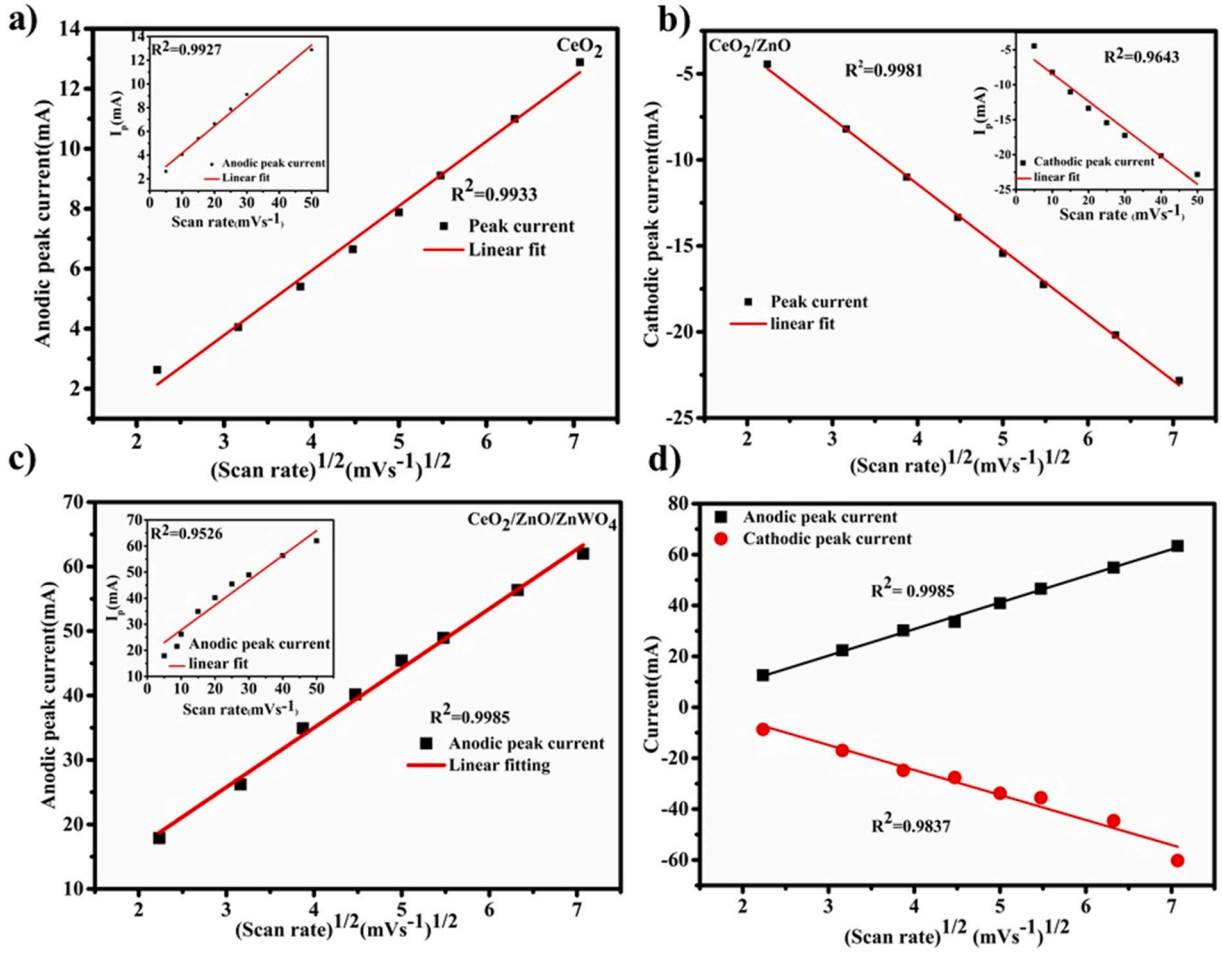

Fig. 9. Diffusion/faradic controlled mechanisms differentiation; I_p vs $\upsilon^{1/2}$ plot, (Inset: I_p vs υ), (a) CeO_2, (b) CeO_2/ZnO, (c) $CeO_2/ZnO/ZnWO_4$, (d) Randles-Sevcik plot for tertiary composite.

$$I_p \propto \upsilon^{1/2} \tag{7}$$

or

$$I_p = Akn^{3/2}\chi(D\upsilon)^{1/2} \tag{8}$$

This is called the Randles-Sevcik equation.

Where I_p = peak current, A = Area of electrode, n = no of electrons in redox reaction, D = diffusion coefficient, k = 2.69×10^5 $Cmol^{-1}$ $V^{-1/2}$, χ = concentration of electro-active species, υ = scan rate (mV/s).

Similarly, for non-diffusion or capacitive mechanisms, the Eq. (9) is used;

$$I_p \propto \upsilon \tag{9}$$

The graphs are plotted (I_p vs $\upsilon^{1/2}$) and (I_p vs υ) to determine the battery grade and capacitive nature of the material and are shown in Fig. 9a–c. The correlation coefficients are obtained by applying linear fitting to the data. The inset graphs in each case show the capacitive response while the main graph depicts the diffusion response of the material. In each case (capacitive and diffusion controlled), the value of R^2 provides the dominant mechanism of charge storage. For CeO_2, the value of R^2 = 0.9927 and 0.9933 which means that both processes contribute equally to the electrochemical signal (Fig. 9a). Similarly, for CeO_2/ZnO composite, R^2 = 0.9981 and 0.9643 for diffusion controlled and surface capacitive response respectively which depicts the dominant feature of battery grade material (Fig. 9b). For tertiary composite, R^2 = 0.9985 and 0.9526 for battery grade (diffusion-controlled process) and surface capacitive response respectively (Fig. 9c). The highest value of R^2 for faradic response indicates that tertiary composite is the best battery grade material among the three materials. [79]. The linear trend is also observed between peak current (I_p) and $\upsilon^{1/2}$ for both anodic and cathodic peaks which is evident in the high reversibility and stable nature of the material as shown in Fig. 9d.

3.2.1. *Evaluation of capacitive and diffusion controlled current for tertiary composite*

The charge storage mechanism varies with the applied scan rate and current density. To evaluate the charge storage mechanism at different scan rates, Donn's model provides us with a new way to probe the different charge storage mechanisms. The current distribution was evaluated by using CV curves for scan rates from 10 to 30 mV/s scan rates [80]. The trend of the charge storage mechanism is evaluated by using the power law (10)–(12);

$$I_p = a\,\upsilon^b \tag{10}$$

or

$$\text{Log } I_p = \text{Log a} + b\,\text{Log}(\upsilon) \tag{11}$$

or

$$\frac{\text{Log Ip}}{\text{Log }\upsilon} = b + \text{Log(a)} \tag{12}$$

where I_p = peak current and υ = scan rate, a = constant, b = constant.

The linear fit between the log (I_p) and Log (υ) provides the nature of the charge of charge storage mechanism. The slop of $\frac{\text{Log Ip}}{\text{Log }\upsilon}$ provides the value of b while the y-intercept gives the Log a. There will be non-

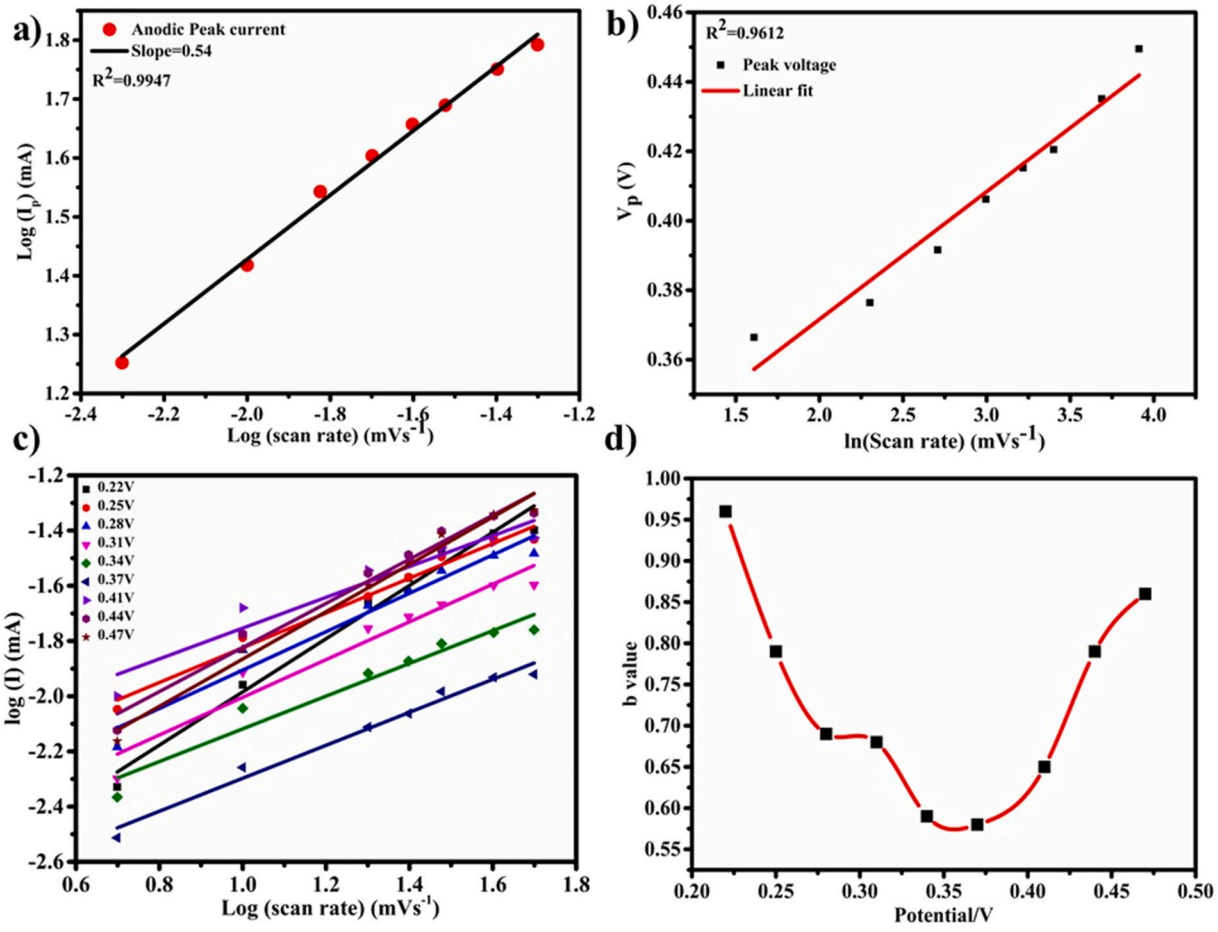

Fig. 10. Charge storage mechanism; (a) Graph between log (peak current) and log (scan rate) to find the value of b, (b) relationship between peak potential versus ln (scan rates), (c) Relationship between log (scan rate) versus log (oxidation and reduction peak currents), (d) Variation of b value at different fixed potentials.

diffusion or capacitive behavior for b = 1, while b = 0.5 represent the diffusion controlled or intercalation process. The linear fit between the log (peak current) and log (scan rate) provides b = 0.54 which indicates the battery grade nature of the material and is consistent with the earlier reported results [81] (Fig. 10a). The linear trend between the peak potential and ln (scan rate) also supports the above results indicating the superior ions charge transfer due to intercalation (Fig. 10b) [82]. The values of b are determined by plotting a graph between current and scan rates at different fixed potentials ranging from 0.22 V to 0.47 V (Fig. 10c). The value of b is 0.96 at the lowest potential which decreases with the rise in potential. The lowest value of b (0.57) is observed at a peak potential of 0.37 V and then increases again with peak potential (Fig. 10d). This variation indicates that current arises from a non-diffusion process which linearly changes into a diffusion-controlled process with the rise in scan rate. At peak potentials, maximum current is attributed to diffusion-controlled process which is due to fast intercalation (ion-exchange process) [83].

In general, both types of current exist during a complete scan process as also observed in our previous discussion. To quantify the intercalative and non-diffusive current, the following Eqs. (13)–(15) are used [84].

$$I(V) = I_{cap} + I_{diff} \tag{13}$$

$$I(V) = K_1 v + K_2 v^{1/2} \tag{14}$$

or

$$I(V)/v^{1/2} = K_1 v^{1/2} + K_2 \tag{15}$$

Thus, by plotting the graph between the $I(V)/v^{1/2}$ and $v^{1/2}$, value of K_1 and K_2 can be determined from the slope and y-intercept of the fitted line respectively as shown in Fig. 11a. It is obvious from Fig. 11b that with an increase in scan rate, intercalation current dominates over the capacitive current which is mainly due to the less time available for diffusion into host lattices. Therefore, at higher scan rates, redox pseudo behavior or intercalation is responsible for the charge storage mechanism [82]. The separation potential between the redox peaks is increased with scan rates which might be due to polarization effects (Fig. 11c) [72].

3.2.2. Galvanostatic charging discharging (GCD)

The charge storage properties of synthesized materials are further studied by using GCD at current densities of 0.5 mAg^{-1}, 1 mAg^{-1}, 3 mAg^{-1}, and 5 mAg^{-1}. GCD curves of different samples are shown in Fig. 12(a–c). From the GCD curves, it is obvious that pristine CeO_2 and CeO_2/ZnO composite depict rectangular shape curves while CeO_2/ZnO/$ZnWO_4$ composite has triangular shape behavior (Fig. 12(a–c)). The triangular pattern of spectrums is an indication of a battery-like charge storage mechanism [73]. The highly conductive tungstate species in ternary composites may be responsible for the negligible potential drop which yields high energy density [85]. The plateaus region in the discharging curve of CeO_2 and CeO_2/ZnO may be attributed to the polarization and ohmic contributions of the material which is also responsible for the shift in redox potential with an increase in current density as shown in (Fig. 12(a–b)) [73]. The specific capacity is also calculated from each discharge curve by using the relation (16)

$$Qs = \frac{I \times \triangle t}{m} \tag{16}$$

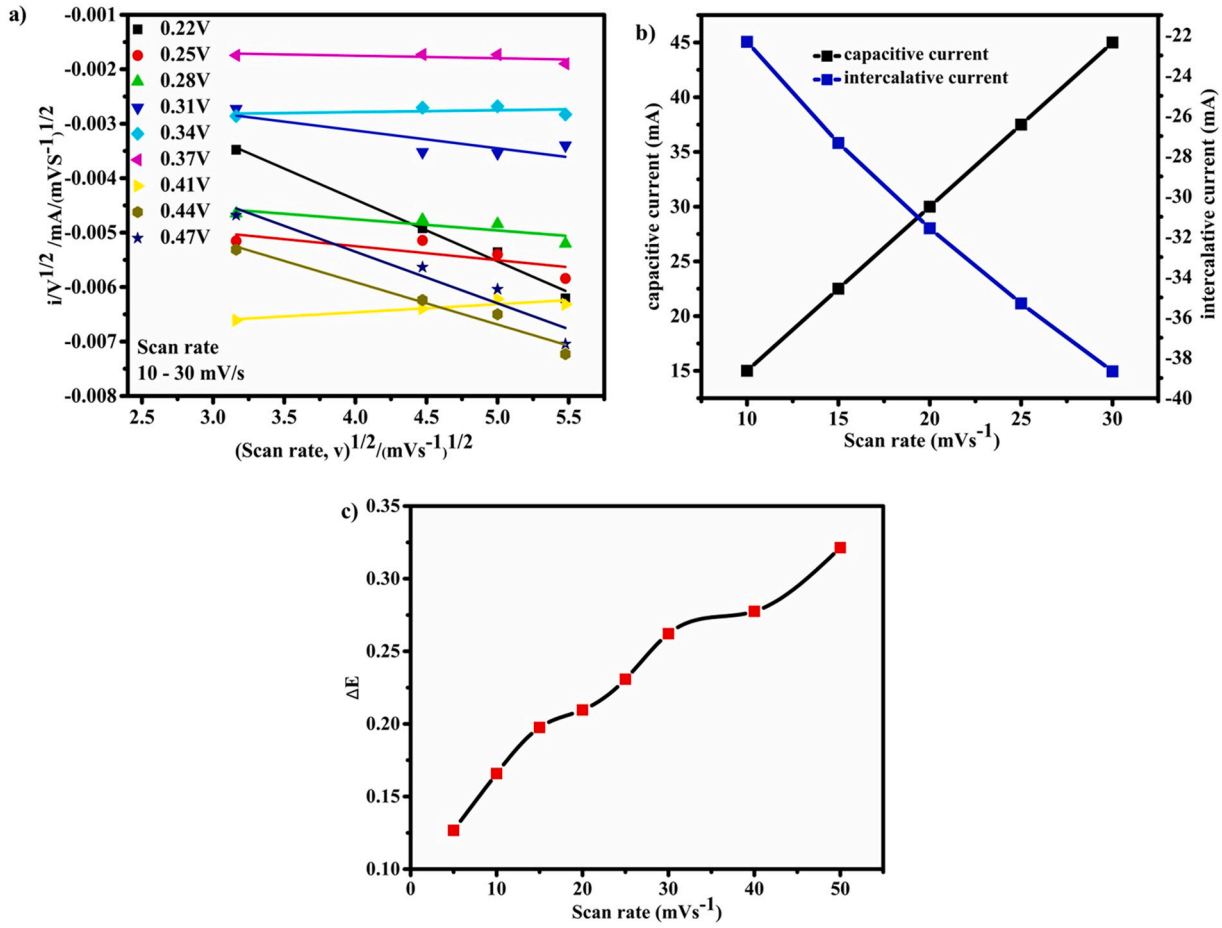

Fig. 11. Charge storage mechanism; (a) graph between $i/v^{1/2}$ and $v^{1/2}$ to find the value of K_1 and K_2, (b) Distribution of current at different scan rates, (c) separation of peak potential versus scan rate.

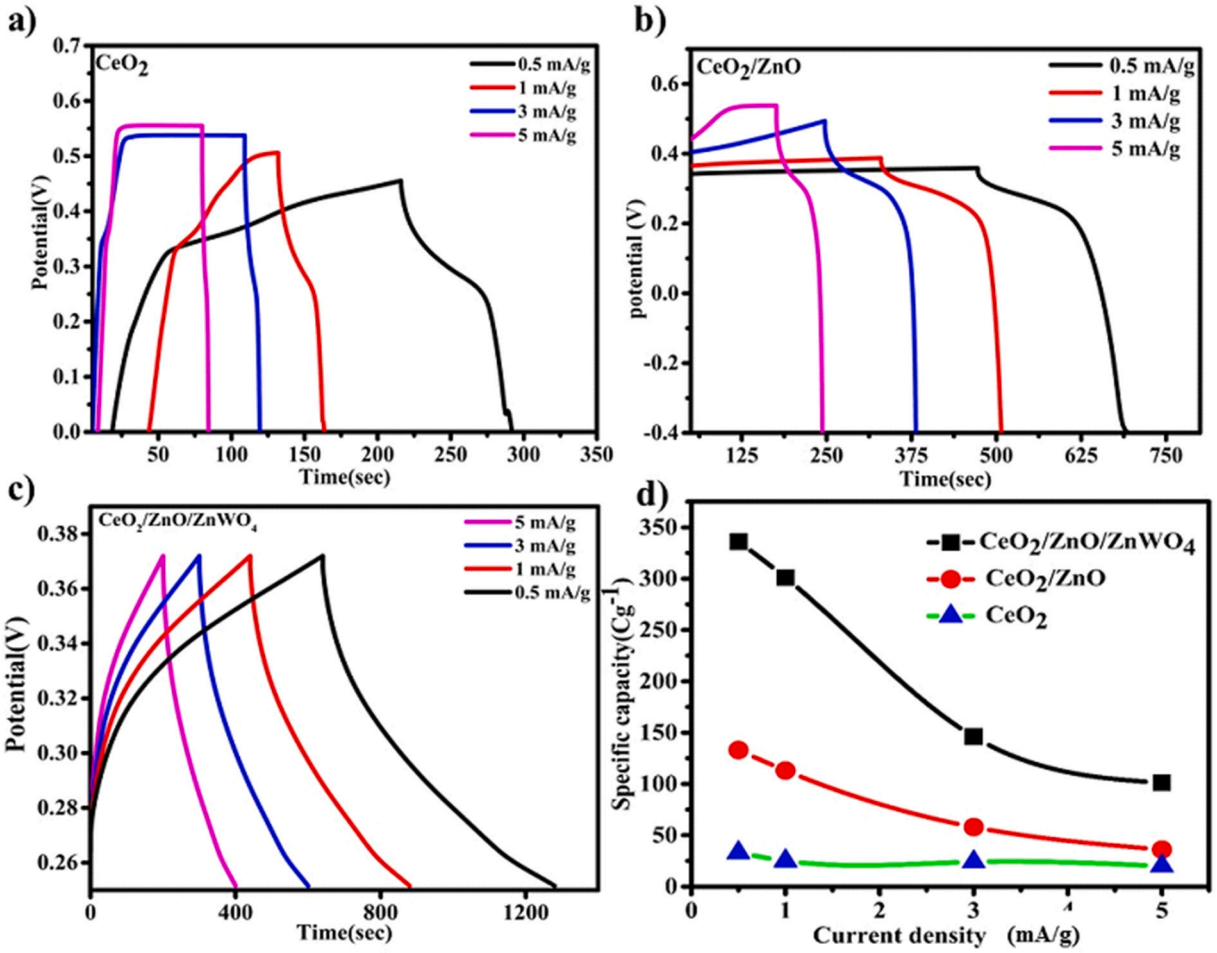

Fig. 12. GCD curves of (a) CeO_2, (b) CeO_2/ZnO, (c) CeO_2/ZnO/$ZnWO_4$, (d) Comparative specific capacity of different materials.

$\triangle t$ = discharging time, I = current density (A), m = mass loaded.

The highest specific capacity is observed for tertiary composite (336 Cg^{-1}) while the minimum specific capacity (33 Cg^{-1}) is observed for pristine CeO_2 at a current density of 1 Ag^{-1}. Fig. 12d shows the trend of specific capacity as a function of current density. The specific capacity decreases significantly due to rapid reaction at the electrode interface thus providing less diffusion of OH^{-1} ions into pores with an increase in current density. The enhancement in the specific capacity for tertiary composite may be attributed to the synergic effects. The presence of tungstate ions (WO_4^{-2}) at the surface provides additional protection from direct exposure of redox species to electrolyte solutions and also enhances conductivity [55]. The presence of WO_4^{-2} ions increases the recombination time of electrons, hence, providing efficient charge transfer [86].

3.2.3. Electrochemical impedance spectroscopy (EIS)

To elucidate the charge process and resistance offered by the electrodes, EIS is performed by varying the frequency from 0.01 to 100 kHz. The Nyquist plot is drawn between real impedance (Z′) versus imaginary impedance (−Z″) (Fig. 13). In the high-frequency region (inset Fig. 13), a small circumference of the circle is observed for tertiary composites which indicates the capacitive nature of the material. In the case of CeO_2, no semicircle is observed which may be due to the rough surface of the electrode or the presence of a non-uniform electric field at the interface of the electrode [69]. The binary (CeO_2/ZnO) and tertiary (CeO_2/ZnO/$ZnWO_4$) composites have almost equal Equivalent Series Resistance (ESR) of 0.63 Ω and 0.65 Ω while CeO_2 has the highest ESR value of 0.81 Ω. The larger value of ESR of CeO_2 may be due to the

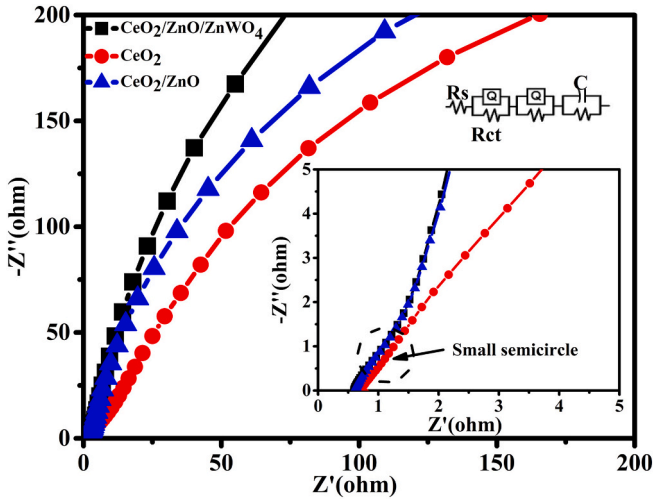

Fig. 13. Nyquist plots of CeO_2 nanosheets, CeO_2/ZnO, and CeO_2/ZnO/$ZnWO_4$ composite, inset: Higher frequency region and equivalent electrical circuit model fitting for tertiary composites.

resistive interface of the electrode. As ESR is the combined effect of solution resistance, electrode-electrolyte interface, and electrode resistance, the lowest value of tertiary composite depicts its highly conductive nature, consistent with the results discussed in the CV and GCD [72]. The mesoporous nature of the electrode allows the electrolytic ions

(OH^{-1}) to interact with the atoms inside the pores thus providing more conducting channels for the transportation of electrons. The linear part in the lower frequency region is called Warburg diffusion impedance (W) associated with the diffusion of ions. The equivalent circuit is shown in the inset Fig. 13 where Rs, R_{ct}, and C depict the solution resistance, charge transfer resistance and capacitor respectively.

3.3. Supercapattery performance of tertiary composites

Since tertiary composite has the highest specific capacity and best faradic nature, therefore, it is further decided to use it for supercapattery application. Activated carbon (AC) and tertiary composites on Ni foam and Whatman filter paper 42 were used as negative, positive, and separators respectively in 2 M KOH electrolyte. The potential window for AC lies from −1 to 0 V while for ternary composite 0–0.7 V. Hence for the optimum performance of the cell, the potential window was selected from −1 to 0.7 V.

For the best performance, it is suggested to balance the charge transfer ratio at cathode and anode, and can be done by using the relation (17);

$$\frac{m_+}{m_-} = \frac{Q_-}{Q_+} = \frac{C_- V_-}{C_+ V_+} \tag{17}$$

where C_-, V_-, C_+, and V_+ are the specific capacitance of the negative electrode, the potential window of the negative electrode, the specific capacitance of the positive electrode, and the potential window of the positive electrode respectively.

The CV is performed on constructed supercapattery for scan rates from 5 mV/s to 30 mV/s as shown in Fig. 14a. No significant change is observed even at faster scan rates which shows the high rate capability of the material. It is also noted that during the negative part of the scan, a small reduction peak is observed which may be attributed to the small pseudo-capacitive behavior of the material [87]. Similarly, the quasi rectangular nature of CV depicts the characteristic double layer capacitor type behavior of the device [88]. The existence of both types of mechanisms is indicating the active participation of both AC and tertiary composite electrodes. The individual CV curves of activated carbon and ternary composite at a scan rate of 30 mVs^{-1} are shown in Fig. 14b.

Furthermore, the energy density and power density are determined by using GCD curves. The shape of the GCD curves of the device is neither completely triangular nor rectangular (Fig. 14c). A small hump is present in the discharging curve as denoted in the GCD curve which shows the pseudo-capacitive behavior while the quasi triangle shape depicts the double layer capacitor behavior [73], consistent with the CV curves (Fig. 14a). The longest discharge time is obtained at the lowest current density due to the high diffusion time of electrolytic ions. Moreover, the potential window does not amend both at high and low current densities which is evident in the negligible interfacial resistance [89] (Fig. 14c). The highest power density of 2000 Wkg^{-1} corresponds to an energy density of 56.92 $Whkg^{-1}$ obtained at a current density of 0.5 mA/g. The comparison of obtained power and energy densties with previous reports is provided in Table 3. In the EIS, the high-frequency region provides the ESR value of 0.96 Ω which shows the high conductivity of the system and hence efficient charge transfer (inset Fig. 14d). The linear part in the low-frequency region (Warburg

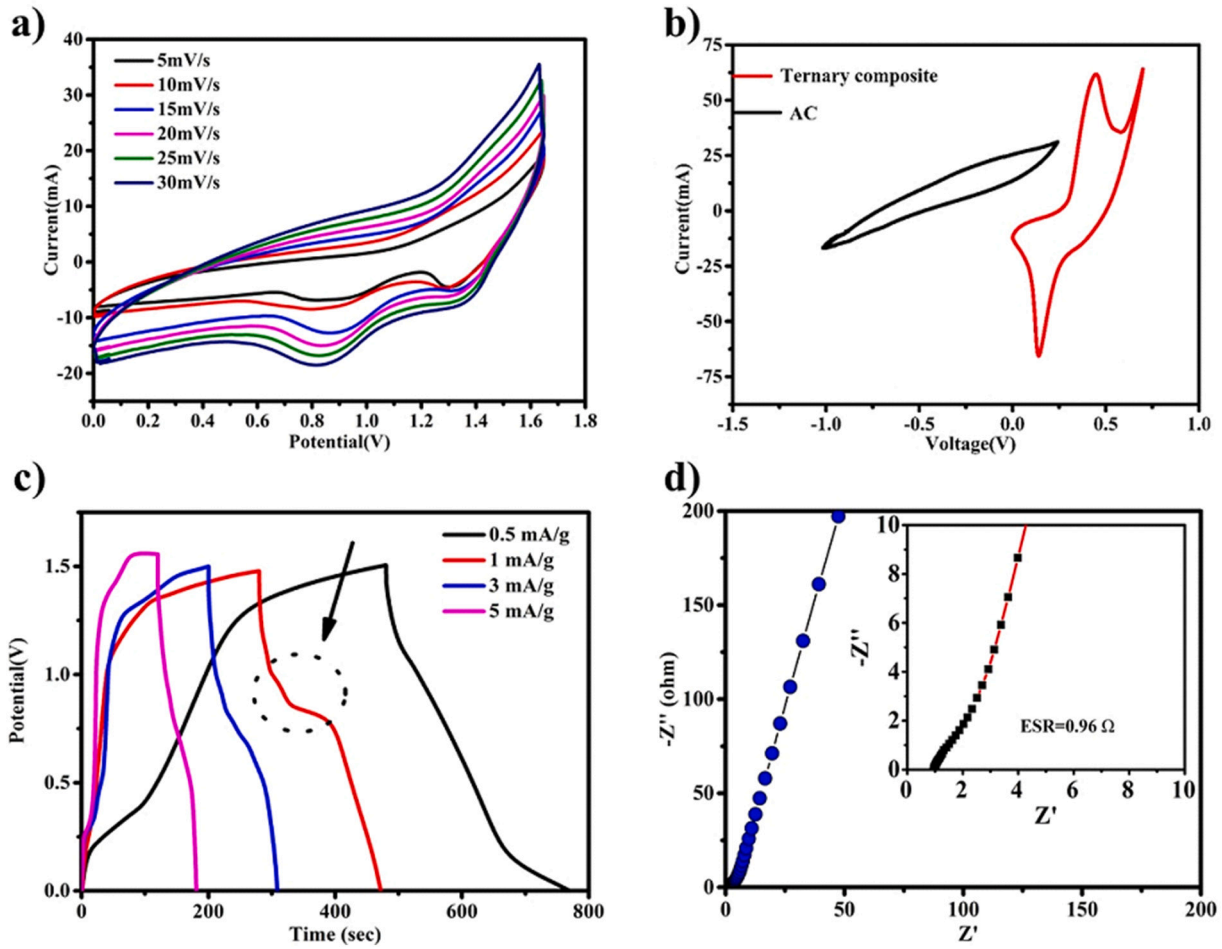

Fig. 14. (a) CV curve of supercapattery, (b) CV curve of ternary composite and activated carbon (AC), (c) GCD curve at various current densities, (d) EIS spectrum of the supercapattery (inset: high-frequency region).

Table 3
Comparison of energy density and power density with reported literature.

Material	Energy density ($Whkg^{-1}$)	Power density (Wkg^{-1})	Reference
$CeO_2/C/MoS_2$	34.55	666.7	[91]
$Ag@CeO_2/AC$	70	750	[92]
CeO_2/rGO	20	500	[93]
$Co/NiWO_4$	42.2	1047.7	[94]
$CoWO_4/Co_3O_4/AC$	57.8	750	[55]
$CeO_2/ZnO/ZnWO_4/AC$	56.92	2000	This work

resistance) is inclined more towards the $-Z''$ indicating the capacitive nature of supercapattery [90] (Fig. 14d). Fig. 15a shows the schematic representation of the supercapattery and its working. The Ragone plot with the comparison of previously reported results is shown in Fig. 15b.

Stability is one of the important factors for device fabrication. The potential remains almost constant before and after 5500 cycles which depicts the high cyclic performance of the device as shown in Fig. 15c. The specific capacity retention and coulombic efficiency are determined for 5500 charging-discharging cycles. The coulombic efficiency is calculated by using Eq. (18);

$$\text{Coulombic efficiency } (\%) = \frac{\Delta t_d}{\Delta t_c} \times 100 \tag{18}$$

where Δt_d and Δt_c discharging and charging time.

There is 88 % retention in specific capacity (Fig. 15d) and 82 % coulombic efficiency is observed after 5500 cycles (inset Fig. 15d). The improved cyclic performance may be attributed to the cooperation of tungstate species (WO_4^{-2}) which not only provide highly conductive channels but also enhance the stability [95] of the device.

In the end, to distinguish the diffusion and surface-controlled capacity contribution, Donn's method is applied as suggested by [96]. Fig. 16(a–c) shows the contribution of both surface and diffusion-controlled capacity at a scan rate of 10 mV/s, 20 mV/s, and 30 mV/s for supercapattery. At 10 mV/s, the capacitive contribution is 28 % of the total capacity while 72 % is based on the diffusion-controlled mechanism (battery grade mechanism), whereas, at 20 and 30 mV/s, the capacitive contribution increases, and the battery type mechanism reduces. The rising trend of the surface-controlled mechanism shows the dominant feature of capacitive behavior at higher scan rates which is due to less diffusion time for electrolytic ions (OH^{-1}). At a faster scan rate, the higher capacitive response is also linked with the major contribution from surface-bound atoms than the inner atoms (Fig. 16d). The contribution of both mechanisms (surface charge adsorption and Faradaic electrochemical reactions) at higher and lower scan rates provide evidence of the successful fabrication of the supercapattery device.

4. Conclusion

In the present study, CeO_2 nanosheet composited with ZnO and $ZnWO_4$ nanomaterials and studied their potential as an electrode in energy storage devices (supercapacitor and supercapattery). The highest specific capacity was obtained (496.9 Cg^{-1}) for tertiary composite at a scan rate of 5 mVs^{-1}. Due to its high specific capacity, the material was used as an electrode in the fabrication of a supercapattery device which showed the highest energy and power density as compared to previously

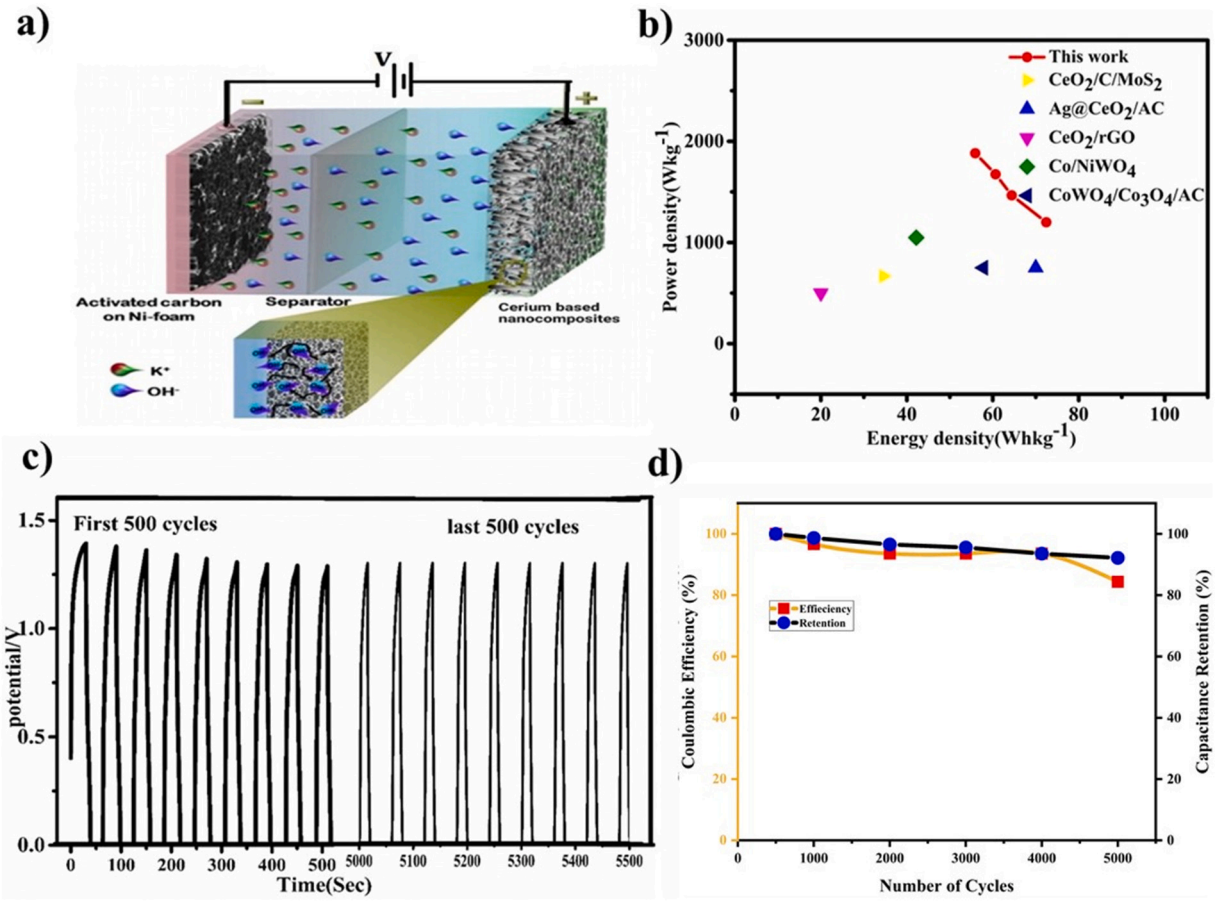

Fig. 15. (a) Schematic illustration of assembled supercapattery device, (b) Ragone plot and comparison with earlier reported literature, (c) GCD cycle of first 500 and last 500 cycles, (d) The percentage retention and coulombic efficiency before and after 5500 cycles.

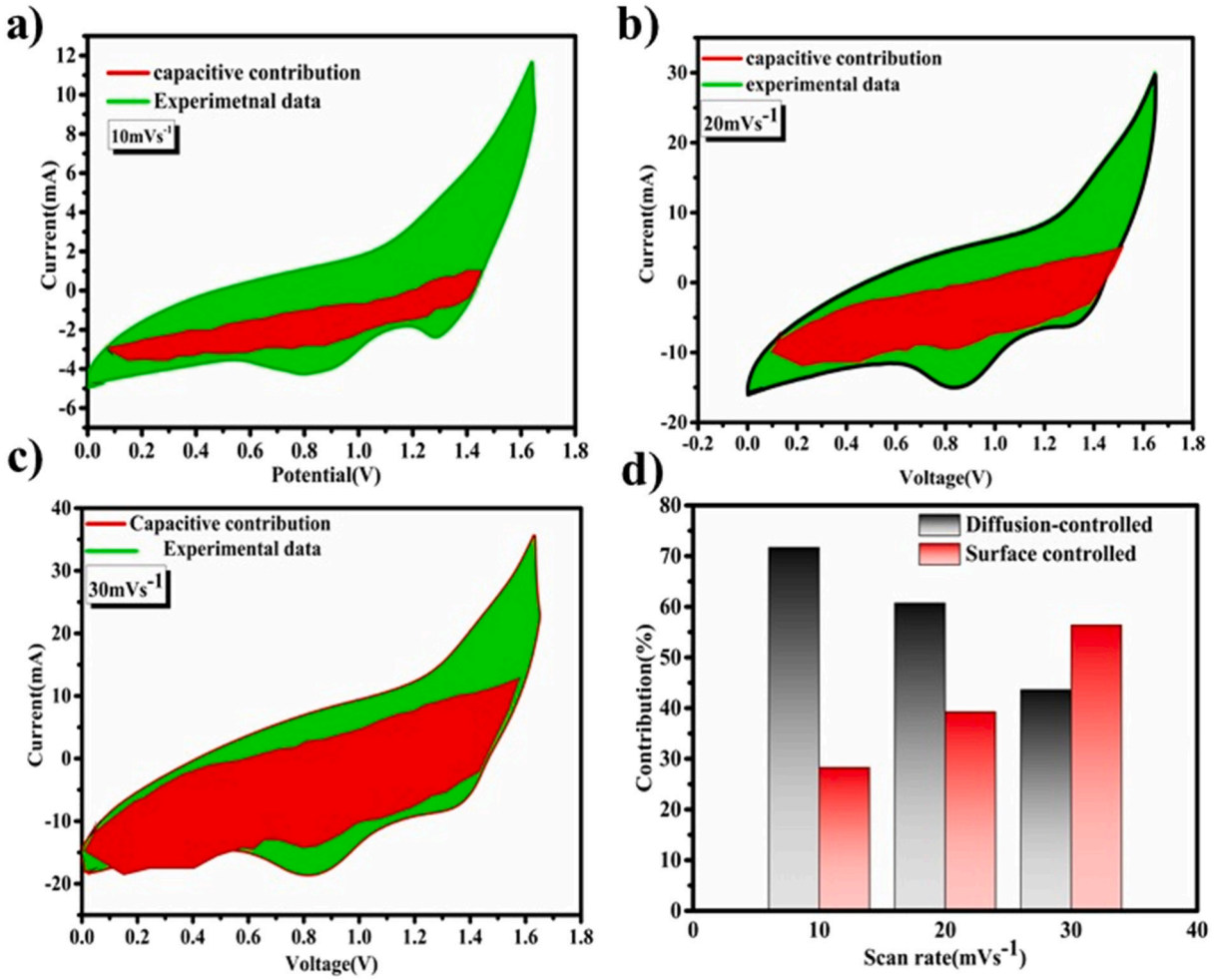

Fig. 16. Capacitive and diffusive capacitance (a) 10 mV/s, (b) 20 mV/s, (c) 30 mV/s, (d) % contribution of surface and diffusion controlled current, (d) Bar graph of diffusion controlled and surface-controlled contribution as a function of scan rate.

reported results. The presence of surface-controlled and diffusion-controlled mechanisms confirmed the asymmetric nature of the super-capattery device. The fabricated devices showed cyclic retention and coulombic efficiency of 88 % and 82 % respectively, showing the stable nature of the material. Thus, from the above-stated results, it can be concluded that 2D materials with tungstate species could be a promising candidate for the utilization of electrode materials for supercapattery devices.

CRediT authorship contribution statement

Muhammad Ramzan Khawar: Writing – original draft, Methodology. **Naveed Akhtar Shad:** Writing – review & editing, Investigation. **Sajad Hussain:** Data curation, Conceptualization, Resources, Funding acquisition. **Yasir Javed:** Supervision, Validation, Resources. **Muhammad Munir Sajid:** Writing – review & editing. **Asim Jilani:** Formal analysis, Resources, Writing – review & editing. **Muhammad Faheem:** Writing – review & editing, Methodology. **Ali Asghar:** Writing – review & editing, Data curation.

Declaration of competing interest

The authors declare that they have no known competing financial interests or personal relationships that could have appeared to influence the work reported in this paper.

Data availability

Data will be made available on request.

Acknowledgments

The authors would like to acknowledge the financial assistance from the Higher Education Commission (HEC) of Pakistan, for providing funds under NRPU Research Project No: 7487/Punjab/NRPU/R&D/HEC/2017.

References

[1] F. Aliyu, T. Sheltami, Development of an energy-harvesting toxic and combustible gas sensor for oil and gas industries, Sensors Actuators B Chem. 231 (2016) 265–275.
[2] J.M. Baptista, J.S. Sagu, U.W. KG, K. Lobato, State-of-the-art materials for high power and high energy supercapacitors: performance metrics and obstacles for the transition from lab to industrial scale–a critical approach, Chem. Eng. J. 374 (2019) 1153–1179.
[3] W. Zhang, A. Maleki, M. Alhuyi Nazari, Optimal operation of a hydrogen station using multi-source renewable energy (solar/wind) by a new approach, J.Energy Storage 53 (2022), 104983.
[4] A. Watil, A. El Magri, R. Lajouad, A. Raihani, F. Giri, Multi-mode control strategy for a stand-alone wind energy conversion system with battery energy storage, J. Energy Storage 51 (2022), 104481.
[5] H. Zhao, N. Hu, R. Xu, H. Liu, J. Liu, Q. Ran, Spray-drying synthesis of LiMnO2@VXC-72R composite microspheres with excellent electrochemical performance, Ceram. Int. 46 (13) (2020) 21805–21809.

[6] H. Zhao, X. Gao, Y. Li, Q. Ran, C. Fu, Y. Feng, J. Liu, X. Liu, J. Su, Synergistic effects of zinc-doping and nano-rod morphology on enhancing the electrochemical properties of spinel Li-Mn-O material, Ceram. Int. 45 (14) (2019) 17591–17597.

[7] H. Zhao, F. Li, X. Shu, J. Liu, T. Wu, Z. Wang, Y. Li, J. Su, Environment-friendly synthesis of high-voltage LiNi0.5Mn1.5O4 nanorods with excellent electrochemical properties, Ceram. Int. 44 (16) (2018) 20575–20580.

[8] H. Zhao, D. Li, Y. Wang, F. Li, G. Wang, T. Wu, Z. Wang, Y. Li, J. Su, Sol-gel synthesis of silicon-doped lithium manganese oxide with enhanced reversible capacity and cycling stability, Materials 11 (8) (2018) 1455.

[9] H. Zhao, F. Li, X. Bai, T. Wu, Z. Wang, Y. Li, J. Su, Enhanced cycling stability of LiCuxMn1.95−xSi0.05O4 cathode material obtained by solid-state method, Materials 11 (8) (2018) 1302.

[10] N.E. Galushkin, N.N. Yazvinskaya, D.N. Galushkin, Nickel-cadmium batteries with pocket electrodes as hydrogen energy storage units of high-capacity, J.Energy Storage 39 (2021), 102597.

[11] M. Wakihara, Recent developments in lithium ion batteries, Mater.Sci.Eng.R: Rep. 33 (4) (2001) 109–134.

[12] S. Kumar, G. Saeed, L. Zhu, K.N. Hui, N.H. Kim, J.H. Lee, 0D to 3D carbon-based networks combined with pseudocapacitive electrode material for high energy density supercapacitor: a review, Chem. Eng. J. 403 (2021), 126352.

[13] Z. Zhu, R. Zhang, J. Lin, K. Zhang, N. Li, C. Zhao, G. Chen, C. Zhao, Ni, Zn-codoped MgCo2O4 electrodes for aqueous asymmetric supercapacitor and rechargeable Zn battery, J. Power Sources 437 (2019), 226941.

[14] J. Li, Y. Zou, L. Jin, F. Xu, L. Sun, C. Xiang, Polydopamine-assisted NiMoO4 nanorods anchored on graphene as an electrode material for supercapacitor applications, J.Energy Storage 50 (2022), 104639.

[15] J. Li, Y. Zou, B. Li, F. Xu, H. Chu, S. Qiu, J. Zhang, L. Sun, C. Xiang, Polypyrrole-wrapped NiCo2S4 nanoneedles as an electrode material for supercapacitor applications, Ceram. Int. 47 (12) (2021) 16562–16569.

[16] Y. Liu, C. Xiang, H. Chu, S. Qiu, J. McLeod, Z. She, F. Xu, L. Sun, Y. Zou, Binary Co–Ni oxide nanoparticle-loaded hierarchical graphitic porous carbon for high-performance supercapacitors, J.Mater.Sci.Technol. 37 (2020) 135–142.

[17] C. Xiang, Q. Wang, Y. Zou, P. Huang, H. Chu, S. Qiu, F. Xu, L. Sun, Simple synthesis of graphene-doped flower-like cobalt–nickel–tungsten–boron oxides with self-oxidation for high-performance supercapacitors, J. Mater. Chem. A 5 (20) (2017) 9907–9916.

[18] J. Xu, X. Yang, Y. Zou, L. Zhu, F. Xu, L. Sun, C. Xiang, J. Zhang, High density anchoring of NiMoS4 on ultrathin Ti3C2 MXene assisted by dopamine for supercapacitor electrode materials, J. Alloys Compd. 891 (2022), 161945.

[19] X. Yang, C. Xiang, Y. Zou, J. Liang, H. Zhang, E. Yan, F. Xu, X. Hu, Q. Cheng, L. Sun, Low-temperature synthesis of sea urchin-like Co-Ni oxide on graphene oxide for supercapacitor electrodes, J.Mater.Sci.Technol. 55 (2020) 223–230.

[20] N. Choudhary, C. Li, J. Moore, N. Nagaiah, L. Zhai, Y. Jung, J. Thomas, Asymmetric supercapacitor electrodes and devices, Adv. Mater. 29 (21) (2017), 1605336.

[21] D. Wu, X. Xie, Y. Ma, J. Zhang, C. Hou, X. Sun, X. Yang, Y. Zhang, H. Kimura, W. Du, Morphology controlled hierarchical NiS/carbon hexahedrons derived from nitrilotriacetic acid-assembly strategy for high-performance hybrid supercapacitors, Chem. Eng. J. 433 (2022), 133673.

[22] D. Wu, X. Xie, J. Zhang, Y. Ma, C. Hou, X. Sun, X. Yang, Y. Zhang, H. Kimura, W. Du, Embedding NiS nanoflakes in electrospun carbon fibers containing NiS nanoparticles for hybrid supercapacitors, Chem. Eng. J. 446 (2022), 137262.

[23] Z.S. Iro, C. Subramani, S. Dash, A brief review on electrode materials for supercapacitor, Int. J. Electrochem. Sci. 11 (12) (2016) 10628–10643.

[24] A. Yu, V. Chabot, J. Zhang, Electrochemical Supercapacitors for Energy Storage And Delivery: Fundamentals And Applications, Taylor & Francis, 2013.

[25] A. Borenstein, O. Hanna, R. Attias, S. Luski, T. Brousse, D. Aurbach, Carbon-based composite materials for supercapacitor electrodes: a review, J. Mater. Chem. A 5 (25) (2017) 12653–12672.

[26] R. Kumar, S.M. Youssry, H.M. Soe, M.M. Abdel-Galeil, G. Kawamura, A. Matsuda, Honeycomb-like open-edged reduced-graphene-oxide-enclosed transition metal oxides (NiO/Co3O4) as improved electrode materials for high-performance supercapacitor, J.Energy Storage 30 (2020), 101539.

[27] I.Y. Bu, R. Huang, Fabrication of CuO-decorated reduced graphene oxide nanosheets for supercapacitor applications, Ceram. Int. 43 (1) (2017) 45–50.

[28] A. Ramadoss, G.-S. Kim, S.J. Kim, Fabrication of reduced graphene oxide/TiO 2 nanorod/reduced graphene oxide hybrid nanostructures as electrode materials for supercapacitor applications, CrystEngComm 15 (47) (2013) 10222–10229.

[29] M. Liu, M. Shi, W. Lu, D. Zhu, L. Li, L. Gan, Core–shell reduced graphene oxide/MnOx@ carbon hollow nanospheres for high performance supercapacitor electrodes, Chem. Eng. J. 313 (2017) 518–526.

[30] G.Z. Chen, Supercapacitor and supercapattery as emerging electrochemical energy stores, Int. Mater. Rev. 62 (4) (2017) 173–202.

[31] D. Mullins, S. Overbury, D. Huntley, Electron spectroscopy of single crystal and polycrystalline cerium oxide surfaces, Surf. Sci. 409 (2) (1998) 307–319.

[32] M. Mazloum-Ardakani, F. Sabaghian, M. Yavari, A. Ebady, N. Sahraie, Enhance the performance of iron oxide nanoparticles in supercapacitor applications through internal contact of α-Fe2O3@ CeO2 core-shell, J. Alloys Compd. 819 (2020), 152949.

[33] Y.H. Leung, M.M. Yung, A.M. Ng, A.P. Ma, S.W. Wong, C.M. Chan, Y.H. Ng, A. B. Djurišić, M. Guo, M.T. Wong, Toxicity of CeO2 nanoparticles–the effect of nanoparticle properties, J. Photochem. Photobiol. B Biol. 145 (2015) 48–59.

[34] A. Trovarelli, Catalytic properties of ceria and CeO2-containing materials, Catal. Rev. 38 (4) (1996) 439–520.

[35] J. Yu, K. Chen, X. Chen, H. Wang, D. Xue, Applying cerium to high performance supercapacitors, Mater.Focus 4 (1) (2015) 81–83.

[36] A. Jeyaranjan, T.S. Sakthivel, C.J. Neal, S. Seal, Scalable ternary hierarchical microspheres composed of PANI/rGO/CeO2 for high performance supercapacitor applications, Carbon 151 (2019) 192–202.

[37] K. Prasanna, P. Santhoshkumar, Y.N. Jo, I.N. Sivagami, S.H. Kang, Y.C. Joe, C. W. Lee, Highly porous CeO2 nanostructures prepared via combustion synthesis for supercapacitor applications, Appl. Surf. Sci. 449 (2018) 454–460.

[38] G.P. Ojha, B. Pant, S.-J. Park, M. Park, H.-Y. Kim, Synthesis and characterization of reduced graphene oxide decorated with CeO2-doped MnO2 nanorods for supercapacitor applications, J. Colloid Interface Sci. 494 (2017) 338–344.

[39] J. Saranya, B. Sreeja, G. Padmalaya, S. Radha, M. Arivanandan, Microwave thermally assisted porous structured cerium oxide/zinc oxide design: fabrication, electrochemical activity towards Pb ions, anticancer assessment in HeLa and VERO cell lines, J. Inorg. Organomet. Polym. Mater. 31 (3) (2021) 1279–1292.

[40] C. Rodwihok, D. Wongratanaphisan, T.V. Tam, W.M. Choi, S.H. Hur, J.S. Chung, Cerium-oxide-nanoparticle-decorated zinc oxide with enhanced photocatalytic degradation of methyl orange, Appl. Sci. 10 (5) (2020) 1697.

[41] M. Mazloum-Ardakani, H. Mohammadian-Sarcheshmeh, H. Naderi, F. Farbod, F. Sabaghian, Fabrication of a high-performance hybrid supercapacitor using a modified graphene aerogel/cerium oxide nanoparticle composite, J.Energy Storage 26 (2019), 100998.

[42] S. Arunpandiyan, S. Bharathi, A. Pandikumar, S.E. Arasi, A. Arivarasan, Structural analysis and redox additive electrolyte based supercapacitor performance of ZnO/CeO2 nanocomposite, Mater. Sci. Semicond. Process. 106 (2020), 104765.

[43] Q. Xie, Y. Zhao, H. Guo, A. Lu, X. Zhang, L. Wang, M.-S. Chen, D.-L. Peng, Facile preparation of well-dispersed CeO2–ZnO composite hollow microspheres with enhanced catalytic activity for CO oxidation, ACS Appl. Mater. Interfaces 6 (1) (2014) 421–428.

[44] Z. Qiao, C. Xia, Y. Cai, M. Afzal, H. Wang, J. Qiao, B. Zhu, Electrochemical and electrical properties of doped CeO2-ZnO composite for low-temperature solid oxide fuel cell applications, J. Power Sources 392 (2018) 33–40.

[45] P. Dhanush, K. Brijesh, S. Vinayraj, H. Nagaraja, High stable zinc tungstate electrode for electrochemical supercapacitor, in: AIP Conference Proceedings, AIP Publishing LLC, 2020.

[46] A. Soultati, A. Verykios, T. Speliotis, M. Fakis, I. Sakellis, H. Jaouani, D. Davazoglou, P. Argitis, M. Vasilopoulou, Organic solar cells of enhanced efficiency and stability using zinc oxide: zinc tungstate nanocomposite as electron extraction layer, Org. Electron. 71 (2019) 227–237.

[47] F. Sedighi, M. Ghiyasiyan-Arani, M. Behpour, Ternary nanocomposites of Ce2W2O9/CoWO4/porous carbon; design, structural study and electrochemical hydrogen storage application, Fuel 310 (2022), 122218.

[48] Y.A. Kumar, G. Mani, M.R. Pallavolu, S. Sambasivam, R.R. Nallapureddy, M. Selvaraj, M. Alfakeer, A.A.A. Bahajjaj, M. Ouladsmane, S.S. Rao, Facile synthesis of highly efficient construction of tungsten disulfide/iron cobaltite nanocomposite grown on nickel foam as a battery-type energy material for electrochemical supercapacitors with superior performance, J. Colloid Interface Sci. 609 (2022) 434–446.

[49] S.R. Ali, M.Z. Iqbal, M.M. Faisal, M. Alzaid, Diffusion control and surface control mechanism in hierarchical nanostructured porous zinc-based MOF material for supercapattery, Int. J. Energy Res. 46 (10) (2022) 14424–14435.

[50] P. Prabakaran, S. Prabhu, M. Selvaraj, M. Navaneethan, P. Ramu, R. Ramesh, Synthesis of r-GO-incorporated CoWO4 nanostructure for high-performance supercapattery applications, J. Mater. Sci. Mater. Electron. 33 (12) (2022) 9312–9323.

[51] X. Fan, Z. Yang, W. Long, B. Yang, J. Jing, R. Wang, The preparation and electrochemical performances of the composite materials of CeO2 and ZnO as anode material for Ni–Zn secondary batteries, Electrochim. Acta 108 (2013) 741–748.

[52] T. Masui, H. Hirai, N. Imanaka, G. Adachi, T. Sakata, H. Mori, Synthesis of cerium oxide nanoparticles by hydrothermal crystallization with citric acid, J. Mater. Sci. Lett. 21 (6) (2002) 489–491.

[53] P. Muhammed Shafi, A. Chandra Bose, Impact of crystalline defects and size on X-ray line broadening: a phenomenological approach for tetragonal SnO2 nanocrystals, AIP Adv. 5 (5) (2015), 057137.

[54] M.S. Javed, S.S.A. Shah, T. Najam, S.H. Siyal, S. Hussain, M. Saleem, Z. Zhao, W. Mai, Achieving high-energy density and superior cyclic stability in flexible and lightweight pseudocapacitor through synergic effects of binder-free CoGa2O4 2D-hexagonal nanoplates, Nano Energy 77 (2020), 105276.

[55] M. Zhang, H. Fan, X. Ren, N. Zhao, H. Peng, C. Wang, X. Wu, G. Dong, C. Long, W. Wang, Study of pseudocapacitive contribution to superior energy storage of 3D heterostructure CoWO4/Co3O4 nanocone arrays, J. Power Sources 418 (2019) 202–210.

[56] P. Prabakaran, S. Prabhu, M. Selvaraj, M. Navaneethan, P. Ramu, R. Ramesh, Synthesis of r-GO-incorporated CoWO4 nanostructure for high-performance supercapattery applications, J. Mater. Sci. Mater. Electron. (2021) 1–12.

[57] Q. Zhang, X. Zhao, L. Duan, H. Shen, R. Liu, Controlling oxygen vacancies and enhanced visible light photocatalysis of CeO2/ZnO nanocomposites, J. Photochem. Photobiol. A Chem. 392 (2020), 112156.

[58] G. Balakrishnan, C. Raghavan, C. Ghosh, R. Divakar, E. Mohandas, J.I. Song, S. Bae, T.G. Kim, X-ray diffraction, Raman and photoluminescence studies of nanocrystalline cerium oxide thin films, Ceram. Int. 39 (7) (2013) 8327–8333.

[59] I.-T. Liu, M.-H. Hon, L.G. Teoh, The preparation, characterization and photocatalytic activity of radical-shaped CeO2/ZnO microstructures, Ceram. Int. 40 (3) (2014) 4019–4024.

[60] Q. Wang, M.M. Sun, C.H. Li, Hydrothermal synthesis and photoluminescent properties of zinc tungstate nano/microstructures, in: Advanced Materials Research, Trans Tech Publ, 2011.

[61] A. Kalinko, A. Kuzmin, Raman and photoluminescence spectroscopy of zinc tungstate powders, J. Lumin. 129 (10) (2009) 1144–1147.
[62] M. Harikrishnan, A.J.C. Mary, A.C. Bose, Electrochemical performance of ANiO3 (A= La, Ce) perovskite oxide material and its device performance for supercapattery application, Electrochim. Acta 362 (2020), 137095.
[63] H. Zhu, P. Zhang, S. Dai, Recent advances of lanthanum-based perovskite oxides for catalysis, ACS Catal. 5 (11) (2015) 6370–6385.
[64] N. Labhasetwar, G. Saravanan, S.K. Megarajan, N. Manwar, R. Khobragade, P. Doggali, F. Grasset, Perovskite-type catalytic materials for environmental applications, in: Sci.Technol.Adv.Mater., 2015.
[65] Q. Hu, B. Yue, F. Yang, H. Shao, J. Wang, L. Ji, Y. Jia, Y. Wang, J. Liu, Facile synthesis and electrochemical properties of perovskite-type CeMnO3 nanofibers, ChemistrySelect 4 (40) (2019) 11903–11912.
[66] C.M. Sims, R.A. Maier, A.C. Johnston-Peck, J.M. Gorham, V.A. Hackley, B. C. Nelson, Approaches for the quantitative analysis of oxidation state in cerium oxide nanomaterials, Nanotechnology 30 (8) (2018), 085703.
[67] A.B. Patil, K.R. Patil, S.K. Pardeshi, Enhancement of oxygen vacancies and solar photocatalytic activity of zinc oxide by incorporation of nonmetal, J. Solid State Chem. 184 (12) (2011) 3273–3279.
[68] S. Prabhu, C. Balaji, M. Navaneethan, M. Selvaraj, N. Anandhan, D. Sivaganesh, S. Saravanakumar, P. Sivakumar, R. Ramesh, Investigation on mesoporous bimetallic tungstate nanostructure for high-performance solid-state supercapattery, J. Alloys Compd. 875 (2021), 160066.
[69] M.M. Faisal, S.R. Ali, M.Z. Iqbal, M.W. Iqbal, A. Numan, K. Sanal, Effect of polyaniline on the performance of zinc phosphate as a battery-grade material for supercapattery, J.Energy Storage 44 (2021), 103329.
[70] N. Padmanathan, S. Selladurai, Shape controlled synthesis of CeO 2 nanostructures for high performance supercapacitor electrodes, RSC Adv. 4 (13) (2014) 6527–6534.
[71] G. He, H. Fan, L. Ma, K. Wang, C. Liu, D. Ding, L. Chen, Dumbbell-like ZnO nanoparticles-CeO2 nanorods composite by one-pot hydrothermal route and their electrochemical charge storage, Appl. Surf. Sci. 366 (2016) 129–138.
[72] A.K. Das, U.N. Pan, V. Sharma, N.H. Kim, J.H. Lee, Nanostructured CeO2/NiV–LDH composite for energy storage in asymmetric supercapacitor and as methanol oxidation electrocatalyst, Chem. Eng. J. 417 (2021), 128019.
[73] T.S. Mathis, N. Kurra, X. Wang, D. Pinto, P. Simon, Y. Gogotsi, Energy storage data reporting in perspective—guidelines for interpreting the performance of electrochemical energy storage systems, Adv. Energy Mater. 9 (39) (2019), 1902007.
[74] C.H. Kim, B.-H. Kim, Zinc oxide/activated carbon nanofiber composites for high-performance supercapacitor electrodes, J. Power Sources 274 (2015) 512–520.
[75] M. Toufani, S. Kasap, A. Tufani, F. Bakan, S. Weber, E. Erdem, Synergy of nano-ZnO and 3D-graphene foam electrodes for asymmetric supercapacitor devices, Nanoscale 12 (24) (2020) 12790–12800.
[76] E. Dhandapani, S. Prabhu, N. Duraisamy, R. Ramesh, Bifunctional copper zinc bimetallic tungstate nanoparticles decorated reduced graphene oxide (CuZnWO4/rGO) for high-performance photocatalytic and supercapacitor application, J. Mater. Sci. Mater. Electron. (2021) 1–14.
[77] L. Fang, Z. Zhang, X. Li, H. Zhou, K. Ma, L. Ge, K. Huang, Fabrication of hybrid cauliflower-like nanoarchitectures by in situ grown ZnO nanoparticals on VS2 ultrathin nanosheets for high performance supercapacitors, Colloids Surf. A Physicochem. Eng. Asp. 501 (2016) 42–48.
[78] G. Zeng, Y. Chen, L. Chen, P. Xiong, M. Wei, Hierarchical cerium oxide derived from metal-organic frameworks for high performance supercapacitor electrodes, Electrochim. Acta 222 (2016) 773–780.
[79] N.S. Punde, A.S. Rajpurohit, A.K. Srivastava, Fabrication of an advanced symmetric supercapattery based on nanostructured bismuth-cobalt-zinc ternary oxide anchored on silicon carbide hybrid composite electrode, Energy Technol. 7 (9) (2019), 1900387.
[80] J. Wang, J. Polleux, J. Lim, B. Dunn, Pseudocapacitive contributions to electrochemical energy storage in TiO2 (anatase) nanoparticles, J. Phys. Chem. C 111 (40) (2007) 14925–14931.
[81] M.Z. Iqbal, M.M. Faisal, S.R. Ali, A.M. Afzal, M.R.A. Karim, M.A. Kamran, T. Alharbi, Strontium phosphide-polyaniline composites for high performance supercapattery devices, Ceram. Int. 46 (8) (2020) 10203–10214.
[82] R. Wang, C. Xu, J.-M. Lee, High performance asymmetric supercapacitors: new NiOOH nanosheet/graphene hydrogels and pure graphene hydrogels, Nano Energy 19 (2016) 210–221.
[83] M. Sathiya, A.S. Prakash, K. Ramesha, J.M. Tarascon, A.K. Shukla, J. Am. Chem. Soc. 133 (2011) 16291–16299.
[84] V. Augustyn, P. Simon, B. Dunn, Pseudocapacitive oxide materials for high-rate electrochemical energy storage, Energy Environ. Sci. 7 (5) (2014) 1597–1614.
[85] S.R. Ede, A. Ramadoss, U. Nithiyanantham, S. Anantharaj, S. Kundu, Bio-molecule assisted aggregation of ZnWO4 nanoparticles (NPs) into chain-like assemblies: material for high performance supercapacitor and as catalyst for benzyl alcohol oxidation, Inorg. Chem. 54 (8) (2015) 3851–3863.
[86] S. Rahimnejad, J.H. He, W. Chen, K. Wu, G.Q. Xu, Tuning the electronic and structural properties of WO 3 nanocrystals by varying transition metal tungstate precursors, RSC Adv. 4 (107) (2014) 62423–62429.
[87] M.Z. Iqbal, M.M. Faisal, S.R. Ali, S. Farid, A.M. Afzal, Co-MOF/polyaniline-based electrode material for high performance supercapattery devices, Electrochim. Acta 346 (2020), 136039.
[88] H. Shi, Activated carbons and double layer capacitance, Electrochim. Acta 41 (10) (1996) 1633–1639.
[89] Q. Li, J. Zhou, R. Liu, L. Han, An amino-functionalized metal–organic framework nanosheet array as a battery-type electrode for an advanced supercapattery, Dalton Trans. 48 (46) (2019) 17163–17168.
[90] M.Z. Iqbal, A. Khan, A. Numan, S.S. Haider, J. Iqbal, Ultrasonication-assisted synthesis of novel strontium based mixed phase structures for supercapattery devices, Ultrason. Sonochem. 59 (2019), 104736.
[91] R. Govindan, X.-J. Hong, P. Sathishkumar, Y.-P. Cai, F.L. Gu, Construction of metal-organic framework-derived CeO2/C integrated MoS2 hybrid for high-performance asymmetric supercapacitor, Electrochim. Acta 353 (2020), 136502.
[92] N. Maheswari, G. Muralidharan, Ag-incorporated CeO 2 nano cauliflowers for high-performance supercapacitor devices, New J. Chem. 41 (19) (2017) 10841–10850.
[93] P.M. Junais, M. Athika, G. Govindaraj, P. Elumalai, Supercapattery performances of nanostructured cerium oxide synthesized using polymer soft-template, J.Energy Storage 28 (2020), 101241.
[94] B. Huang, H. Wang, S. Liang, H. Qin, Y. Li, Z. Luo, C. Zhao, L. Xie, L. Chen, Two-dimensional porous cobalt–nickel tungstate thin sheets for high performance supercapattery, Energy Storage Mater. 32 (2020) 105–114.
[95] S. Alam, M.Z. Iqbal, N. Amjad, R. Ali, M. Alzaid, Magnetron sputtered tungsten di-sulfide: an efficient battery grade electrode for supercapattery devices, J.Energy Storage 46 (2022), 103861.
[96] T. Brezesinski, J. Wang, J. Polleux, B. Dunn, S.H. Tolbert, Templated nanocrystal-based porous TiO2 films for next-generation electrochemical capacitors, J. Am. Chem. Soc. 131 (5) (2009) 1802–1809.